Ultrasonics 166 (2026) 108102

Contents lists available at ScienceDirect

Ultrasonics

journal homepage: www.elsevier.com/locate/ultras

Analytical framework for modelling body-wave scattering and diffusion in concrete

Hao Cheng [a,*], Katrin Löer [b], Max A.N. Hendriks [a,c], Yuguang Yang [a]

[a] Department of Engineering Structures, Faculty of Civil Engineering and Geosciences, Delft University of Technology, 2628 CN Delft, the Netherlands
[b] Department of Geoscience and Engineering, Faculty of Civil Engineering and Geosciences, Delft University of Technology, 2628 CN Delft, the Netherlands
[c] Department of Structural Engineering, Faculty of Engineering, Norwegian University of Science and Technology, 7491 Trondheim, Norway

ARTICLE INFO

Keywords:
Concrete
Diffuse waves
Heterogeneous materials
Multiple scattering

ABSTRACT

This work presents a concrete-specific analytical framework for modelling body-wave scattering by explicitly tailoring multiple-scattering theory to the microstructural characteristics of concrete. Instead of treating scattering parameters as abstract statistical quantities, the framework parameterizes the key inputs of scattering theory in terms of physically measurable concrete attributes, including coarse aggregate size, volume fraction, and the material property contrast between the matrix and the dominant scattering phase, whether coarse aggregates or the interfacial transition zone. By embedding these microstructure-informed parameters into a two-phase spatial statistical formulation, closed-form expressions for total and transport scattering cross-sections are derived and directly linked to ultrasonic diffusivity through diffuse wave theory. Experimental validation using geopolymer concrete members and published data for ordinary concrete demonstrates consistent agreement between theoretical predictions and experimental measurements across a broad frequency range. The proposed framework therefore renders body-wave scattering in concrete quantitatively computable from material composition, providing a physically grounded basis for quantitative interpretation of diffuse wave transport, energy equilibration, and coda-wave velocity changes without reliance on ad hoc fitting parameters.

1. Introduction

Monitoring concrete structures using ultrasonic techniques has received increasing attention in recent decades due to the intrinsic relationship between wave velocity and mechanical properties of the material [1]. Conventional ultrasonic methods rely on measuring the velocity of longitudinal or transverse waves, deduced from the time-of-flight of an ultrasonic pulse, to assess the integrity of the material [2]. However, this approach has limitations, such as only detecting changes along the wave path and requiring high-frequency waves to identify early-stage defects. As a promising alternative, the use of diffuse waves for concrete structure monitoring has gained considerable interest [3–6].

Diffuse waves refer to elastic waves in the diffusive regime, where the wavefield evolves into an approximately randomized state in terms of propagation and polarization direction as a result of multiple scattering, thereby losing phase information and propagation direction of the original incident wave [7,8]. Because such randomization requires numerous scattering events, diffuse waves typically do not appear in the early part of the signal, as the first arrivals consist mainly of coherent waves that travel directly from the source to the receiver with minimal scattering [9]. As the later portion of the signal accumulates multiply scattered energy, diffuse waves become dominant in the coda [10,11]. The wavefield of diffuse waves is often treated as randomized in the diffuse limit, meaning the wave energy becomes approximately equipartitioned between longitudinal and transverse modes in a statistical sense, with longitudinal and transverse waves arriving from all directions at approximately equal intensity [12]. Despite the random nature of the diffuse wave field, the transport of the diffuse wave energy [13–16] can be described using the diffusion equation [17] under the usual assumptions of the diffusive regime. Furthermore, the ratio of transverse to longitudinal wave energy in diffuse body waves converges to a constant, independent of the scattering process, a phenomenon known as energy equilibration [18–20].

The practical relevance of diffuse waves lies in their high sensitivity to subtle changes in the medium and their ability to sample large regions [21]. The former arises from their long, multiply scattered paths, which cause tiny perturbations in the medium to accumulate, while the latter results from these extended trajectories enabling the waves to probe a

* Corresponding author.
E-mail address: haojaysonshing@gmail.com (H. Cheng).

https://doi.org/10.1016/j.ultras.2026.108102
Received 5 January 2026; Received in revised form 17 March 2026; Accepted 13 April 2026
Available online 28 April 2026

Nomenclature

Roman upper case

A_{ij}, [−] Contrast factor between matrix and scatterer properties (i and j can be the material parameters ρ, μ and λ)
$A_i^{(m)}$, [kg/m^3] (ρ) or [N/m^2] (μ, λ) Magnitude of the material property of the matrix (i can be ρ, μ and λ)
$A_i^{(s)}$, [kg/m^3] (ρ) or [N/m^2] (μ, λ) Magnitude of the material property of the scatterer (i can be ρ, μ and λ)
D, [m^2/s] Diffusivity
E, [a.u.] Transport energy (in arbitrary units)
E_0, [a.u.] Deposited impulse energy at the initial location at time $t = 0$ (in arbitrary units)
L_S, [m] Length of the concrete sample
H, [m] Characteristic correlation length
H_S, [m] Height of the concrete sample
I_m, [−] Random field of matrix phase
I_s, [−] Random field of scatterer phase
K_m, [−] Matrix phase in the two-phase medium
K_s, [−] Scatterer phase in the two-phase medium
R, [−] Normalized correlation function
R_{ij}, [−] Correlation function of material-property fluctuations between i and j (i and j can be the material parameters ρ, μ and λ)
$\widetilde{R}_{ij}^{KL}$, [m^3] Power spectral density (PSD) of material-property fluctuations between i and j (i and j can be the material parameters ρ, μ and λ) for incident wave mode K and scattered wave mode L (K and L can be either longitudinal waves or transverse waves)
V, [m^3] Total volume of coarse aggregates
W_S, [m] Width of the concrete sample

Roman lower case

$\mathbf{a}_R$, [m] Position vectors of the receiver with coordinates (x_R,y_R,z_R)
$\mathbf{a}_S$, [m] Position vector of the source with coordinates (x_S,y_S,z_S)
d_s, [m] Diameter of a single scatterer
f, [Hz] Hertz frequency
g, [−] Total amount of grading intervals for coarse aggregates
k_M, [m^{-1}] Wavenumber of wave mode M (M can be either longitudinal waves or transverse waves)
$\mathbf{k}_K$, [m^{-1}] Incident wave vector (K can be either longitudinal waves or transverse waves)
$\mathbf{k}_L$, [m^{-1}] Scattered wave vector (L can be either longitudinal waves or transverse waves)
l^*_M, [m] Transport mean free path of wave mode M (M can be either longitudinal waves or transverse waves)
n_i, [−] Volume ratio of coarse aggregate within the grading interval i
$\mathbf{p}$, [−] Unit wave vector indicating the propagation direction of the incident wave
$\mathbf{p}$', [−] Unit wave vector indicating the propagation direction of the scattered wave
r, [m] Distance between two locations $\mathbf{x}_1$ and $\mathbf{x}_2$
r_c, [m] Characteristic radius for monodisperse spherical scatterers
r_i, [m] Characteristic radius of coarse aggregates within the grading interval i
r_s, [m] Characteristic radius of coarse aggregates
t, [s] Time
v, [m^3] Volume associated with aggregates of a certain radius
v_M, [m/s] Velocity of wave mode M (M can be either longitudinal waves or transverse waves)
$\mathbf{x}$, [m] Spatial vector
x_M, [−] Dimensionless frequency for wave mode M (M can be either longitudinal waves or transverse waves)

Greek upper case

Σ_{KL}, [m^{-1}] Total scattering cross-section associated with mode transition from incident wave mode K to scattered wave mode L (K and L should be either longitudinal waves or transverse waves)
Σ_{KL}', [m^{-1}] Weighted total scattering cross-section associated with mode transition from incident wave mode K to scattered wave mode L (K and L can be either longitudinal waves or transverse waves)

Greek lower case

θ_s, [rad] Scattering angle between incident and scattered wave directions
λ, [N/m^2] Lamé first constant
μ, [N/m^2] Lamé second constant
ρ, [kg/m^3] Mass density
σ, [s^{-1}] Dissipation
σ_{KL}, [m^{-1}] Scattering cross-section associated with mode transition from incident wave mode K to scattered wave mode L (K and L can be either longitudinal waves or transverse waves)
χ, [−] Cosine of the scattering angle
ϕ_m [−] Volume fraction of matrix
ϕ_s, [−] Volume fraction of scatterers
ω, [rad/s] Angular frequency

much larger spatial volume than ballistic waves. These capabilities have driven increasing adoption of diffuse waves in concrete non-destructive testing (NDT) and structural health monitoring (SHM), such as early damage characterization [22–27], stress change detection [28–31], thermal effects [32–35], and crack imaging using sparse sensor networks [36–40]. However, despite these successful demonstrations, a large fraction of diffuse-wave-based studies remains qualitative rather than quantitative, in part because the underlying scattering mechanisms governing diffuse wave behaviour remain insufficiently understood in concrete.

In the diffusive regime, key observable quantities such as diffusivity [41], the spreading velocity of the diffusion halo, and the equilibrated longitudinal–transverse wave energy ratio are not independent parameters; current scattering theory shows that they are determined by the total and transport scattering cross-sections of the medium [14,20,42,43]. To our knowledge, an established analytical framework for concrete has not yet been reported that simultaneously takes measurable microstructural inputs, computes body-wave scattering cross-sections, and links them to diffusivity within a single workflow. As a result, variations in diffusivity cannot be straightforwardly related to microstructural attributes. Additionally, the energy equilibration process in concrete, including its final equilibrated ratio and the time required to reach equilibration, remains difficult to predict quantitatively. This lack of quantitative knowledge of energy equilibration is particularly restrictive for coda-wave-based stress evaluation: the velocity change observed in the coda is essentially a weighted average of longitudinal and transverse wave velocities with their energy ratio as weights [15]. Without the equilibrated energy ratio, these velocity changes cannot be converted into meaningful stress changes, leaving current coda-based imaging results limited to reconstructing velocity change fields rather than stress change fields [36].

Limited attempts have been made to address body-wave scattering in concrete. Anugonda et al. [44] first applied a general multiple-scattering framework to concrete, but the lack of explicit procedures for

determining concrete-specific microstructural parameters limited its direct applicability in practice. Subsequent studies, such as those by Ramaniraka et al. [34,35], have shown that scattering in ordinary concrete is strongly influenced by the interfacial transition zone (ITZ) surrounding coarse aggregates. However, they did not provide a direct analytical route linking scattering behaviour to experimentally inferred diffusivity within the same framework, making direct diffusivity-based validation difficult. A recent review by Darmon et al. [45] highlighted the need for more concrete-specific ultrasonic scattering models that account for realistic microstructure, while the link to diffuse-wave observables such as experimentally inferred diffusivity remains largely undeveloped. This lack of a concrete-specific scattering framework hinders a fully quantitative formulation of scattering in concrete and consequently limits the establishment of theoretical links between scattering, diffusivity, and the energy-equilibration process in diffuse-processes in heterogeneous solids [51,52].

To account for possible mode conversions during wave-scatterer interactions, scattering cross-sections for a given incident wave mode are subdivided into components that preserve the original mode and those that convert it to another mode. For longitudinal waves, these are denoted as σ_{PP} and σ_{PS}, where the first letter indicates the incident mode and the second the scattered one. The corresponding total scattering cross-sections, also known as longitudinal wave attenuations [46], are denoted as Σ_{PP} and Σ_{PS}. An analogous notation is used for transverse waves. Explicit expressions for the total scattering cross-sections in heterogeneous solids require rigorous derivation. In this work, the formulations given by Turner and Anugonda [46] are adopted. The mode-conversion-related total scattering cross-sections are expressed as [46]:

$$\Sigma_{PP} = \int_{-1}^{+1} \sigma_{PP}(\chi)\mathrm{d}\chi \ ,$$
$$\sigma_{PP}(\chi) = \frac{\pi^2\omega^4}{v_P^4}\left[\frac{\left(v_P^2-2v_S^2\right)^2}{v_P^4}\widetilde{R}_{\lambda\lambda}^{PP}(\chi) + \frac{2\left(v_P^2-2v_S^2\right)}{v_P^2}\chi\widetilde{R}_{\lambda\rho}^{PP}(\chi) + \frac{4v_S^2\left(v_P^2-2v_S^2\right)}{v_P^4}\chi^2\widetilde{R}_{\lambda\mu}^{PP}(\chi) + \chi^2\widetilde{R}_{\rho\rho}^{PP}(\chi) + \frac{4v_S^2}{v_P^2}\chi^3\widetilde{R}_{\rho\mu}^{PP}(\chi) + \frac{4v_S^4}{v_P^4}\chi^4\widetilde{R}_{\mu\mu}^{PP}(\chi)\right] \ , \tag{1a}$$

wave-based NDT and SHM.

This paper introduces an analytical framework for modelling body-wave scattering and diffusion in concrete by explicitly accounting for the contributions of coarse aggregates and the surrounding interfacial transition zone (ITZ). The development begins with the general multiple-scattering theory of Turner and Anugonda [46], which is presented in Section 2, and then evolves in Section 3 into a concrete-specific formulation by defining the necessary microstructural parameters and establishing an explicit procedure for computing total scattering cross-sections. With these elements in place, the framework connects the derived scattering properties to body-wave diffusivity, enabling a quantitative link between concrete microstructure and wave transport. The performance of the proposed framework is examined in Section 4 through comparisons with experimental measurements and published data, while Section 5 consolidates the assumptions, limitations, and potential extensions of the approach.

$$\Sigma_{SS} = \int_{-1}^{+1} \sigma_{SS}(\chi)\mathrm{d}\chi \ ,$$
$$\sigma_{SS}(\chi) = \frac{\pi^2\omega^4}{2v_S^4}\left[\left(1-3\chi^2+4\chi^4\right)\widetilde{R}_{\mu\mu}^{SS}(\chi) + \left(\chi^2+1\right)\widetilde{R}_{\rho\rho}^{SS}(\chi) + 4\chi^3\widetilde{R}_{\rho\mu}^{SS}(\chi)\right] \ , \tag{1b}$$

$$\Sigma_{PS} = \int_{-1}^{+1} \sigma_{PS}(\chi)\mathrm{d}\chi \ ,$$
$$\sigma_{PS}(\chi) = \frac{\pi^2\omega^4}{v_S^3 v_P}\left[\left(1-\chi^2\right)\widetilde{R}_{\rho\rho}^{PS}(\chi) + \frac{4v_S}{v_P}\chi\left(1-\chi^2\right)\widetilde{R}_{\rho\mu}^{PS}(\chi) + \frac{4v_S^2}{v_P^2}\chi^2\left(1-\chi^2\right)\widetilde{R}_{\mu\mu}^{PS}(\chi)\right] , \tag{1c}$$

$$\Sigma_{SP} = \int_{-1}^{+1} \sigma_{SP}(\chi)\mathrm{d}\chi \ ,$$
$$\sigma_{SP}(\chi) = \frac{\pi^2\omega^4}{2v_P^3 v_S}\left[\left(1-\chi^2\right)\widetilde{R}_{\rho\rho}^{SP}(\chi) + \frac{4v_S}{v_P}\chi\left(1-\chi^2\right)\widetilde{R}_{\rho\mu}^{SP}(\chi) + \frac{4v_S^2}{v_P^2}\chi^2\left(1-\chi^2\right)\widetilde{R}_{\mu\mu}^{SP}(\chi)\right] , \tag{1d}$$

2. Analytical expressions for multiple scattering of body waves in heterogeneous solids

To establish the analytical basis needed for concrete, we begin with the general theory of multiple scattering in heterogeneous media. When elastic waves propagate through a heterogeneous medium, they interact repeatedly with embedded heterogeneities. These interactions redirect part of the wave energy into new directions, a process known as *scattering*, and may also trigger conversions between wave modes [15]. The scattering discussed here pertains specifically to elastic scattering [42,47,48], where energy conservation holds throughout the scattering process. To quantify the angular distribution of the scattered energy, the scattering angle θ_s is introduced and defined as the angle between the incident unit wave vector $\mathbf{p}$ (indicating the propagation direction of the incident wave) and the scattered unit wave vector $\mathbf{p'}$ (indicating the propagation direction of the scattered wave). Their dot product provides $\cos\theta_s$. The scattering plane is determined by $\mathbf{p}$ and $\mathbf{p'}$, and the scattered spherical wave can be locally treated as a plane wave [49]. The *scattering cross-section* is defined as a measure of the energy flux scattered into a given direction specified by θ_s [50], and the *total scattering cross-section* is obtained by integrating this quantity over all solid angles [20]. As such, the total scattering cross-section offers a compact quantitative measure of the cumulative scattering strength experienced by a wave and therefore serves as a key analytical descriptor of multiple scattering

where ω represents the angular frequency; v_P and v_S denote average longitudinal wave and transverse wave velocities; and ρ is the average density. The parameter χ is defined as the cosine of the scattering angle, $\cos\theta_s$, between the incident wave vector $\mathbf{k}_K=(\omega/v_K)\mathbf{p}$ and scattered wave vector $\mathbf{k}_L=(\omega/v_L)\mathbf{p'}$, where superscripts K and L (K, L$\in${P,S}) denote incident and scattered wave modes. The power spectral density (PSD) of material-property fluctuations $\widetilde{R}_{ij}^{KL}(\chi)$ appearing in Equation (1) is defined as [46]:

$$\widetilde{R}_{ij}^{KL}(\chi) := \widetilde{R}_{ij}^{KL}(|\boldsymbol{k}_K - \boldsymbol{k}_L|) \ , \tag{2}$$

where the subscripts i and j can denote density ρ, Lamé first parameter λ and Lamé second parameter μ. For example, $\widetilde{R}_{\lambda\lambda}$ is the PSD of fluctuations of λ, and $\widetilde{R}_{\lambda\mu}$ is the cross power spectral density (CPSD) of fluctuations of λ and μ. The expressions in Equation (1) correspond to wave energy and are therefore twice those associated with displacement [46].

Although these analytical expressions rigorously describe multiple scattering in heterogeneous solids, directly measuring total scattering cross-sections in laboratory or field experiments is extremely challenging. Consequently, geophysical studies typically infer scattering properties indirectly, for example from coda attenuation Q_c [53] or from the evolution of seismic energy envelopes [54,55]. In the diffuse regime, the envelope can be modelled using the diffusion equation, from which the diffusivity can be estimated as an effective measure of scattering

strength. This diffusivity is not an ad hoc parameter; its connection to the underlying scattering cross-sections is provided analytically by Weaver [42] and Turner [20]. This theoretical link allows the scattering cross-sections to serve as the fundamental parameters governing wave transport in the diffuse regime. On this basis, once the total scattering cross-sections are known, the transport lengths for longitudinal and transverse waves, defined as the characteristic distances over which a wave loses memory of its initial propagation direction [56] and commonly referred to as the *transport mean free path* [20,46], are given by [20,41,46]:

$$l_{\mathrm{P}}^{*}=\frac{\Sigma_{\mathrm{SS}}+\Sigma_{\mathrm{SP}}-\Sigma_{\mathrm{SS}}^{'}+\Sigma_{\mathrm{PS}}^{'}}{\left(\Sigma_{\mathrm{PP}}+\Sigma_{\mathrm{PS}}-\Sigma_{\mathrm{PP}}^{'}\right)\left(\Sigma_{\mathrm{SS}}+\Sigma_{\mathrm{SP}}-\Sigma_{\mathrm{SS}}^{'}\right)-\Sigma_{\mathrm{PS}}^{'}\Sigma_{\mathrm{SP}}^{'}}\quad , \tag{3a}$$

$$l_{\mathrm{S}}^{*}=\frac{\Sigma_{\mathrm{PP}}+\Sigma_{\mathrm{PS}}-\Sigma_{\mathrm{PP}}^{'}+\Sigma_{\mathrm{SP}}^{'}}{\left(\Sigma_{\mathrm{PP}}+\Sigma_{\mathrm{PS}}-\Sigma_{\mathrm{PP}}^{'}\right)\left(\Sigma_{\mathrm{SS}}+\Sigma_{\mathrm{SP}}-\Sigma_{\mathrm{SS}}^{'}\right)-\Sigma_{\mathrm{PS}}^{'}\Sigma_{\mathrm{SP}}^{'}}\quad , \tag{3b}$$

where Σ' is the *transport scattering cross-section* [42], a weighted version of the total scattering cross-section with weights determined by $\cos\theta_{\mathrm{s}}$. The diffusivity of body waves is then expressed as [20,41,46,47]:

$$D=\frac{v_{\mathrm{S}}^{3}\left(\frac{1}{3}v_{\mathrm{P}}l_{\mathrm{P}}^{*}\right)+2v_{\mathrm{P}}^{3}\left(\frac{1}{3}v_{\mathrm{S}}l_{\mathrm{S}}^{*}\right)}{2v_{\mathrm{P}}^{3}+v_{\mathrm{S}}^{3}}\quad . \tag{4}$$

3. Parameter identification for applying the analytical framework to concrete

Although the analytical expressions in Section 2 provide a complete framework for describing multiple scattering and energy transport in heterogeneous solids, their application to concrete requires quantities that are not yet specified. In particular, evaluating the total scattering cross-sections in Equation (1) demands the PSD and CPSD of material-property fluctuations. These quantities are abstract descriptors in the general theory but must be defined explicitly from the characteristics of concrete before the framework can be used in practice. The purpose of Section 3 is therefore to connect the general analytical framework to concrete by establishing these material-specific parameters. To streamline the calculation, we model concrete as a binary material containing monodisperse, spherical scatterers that are uniformly and randomly distributed in space.

3.1. Statistical representation of simplified two-phase concrete for PSD/CPSD derivation

Directly obtaining the PSD/CPSD of material-property fluctuations required in Equation (1) in the Fourier domain is not feasible. Hence, a more viable approach involves initially acquiring the spatial correlation function of material-property fluctuations and subsequently transforming it into PSD or CPSD through Fourier transform operation. The spatial correlation function, which quantifies the spatial statistics of material properties in a heterogeneous medium, is used to link spatial fluctuations of elastic parameters to the dynamic properties of elastic waves [57]. To simplify the concrete in the following derivation, this material is treated as a two-phase or binary material: scatterers and the matrix. Investigating the spatial correlation function in this material is not a new topic. The earliest attempt can be dated back to 1949 by Debye and Bueche [58]. Since then, the related theory has been further developed [59] and has been widely applied in the construction of random media [60–62].

For the assumed two-phase concrete, the entirely three-dimensional space can be divided into two non-intersecting parts: the scatterer phase $\mathrm{K_s}$ and the matrix phase $\mathrm{K_m}$. The random field of scatterers in the two-phase material is:

$$I_{\mathrm{s}}(\boldsymbol{x})=\begin{cases}1, & \text{if } \boldsymbol{x}\in \mathrm{K_s}\\ 0, & \text{otherwise}\end{cases}\quad . \tag{5}$$

Here $I_{\mathrm{s}}(x)$ denotes a binary-valued indicator function of the scatterer phase, defined on a continuous spatial domain. Consequently, the random field of the matrix phase is $I_{\mathrm{m}}(\mathbf{x}) = 1\text{-}I_{\mathrm{s}}(\mathbf{x})$. The ensemble averages of $I_{\mathrm{s}}(\mathbf{x})$ and $I_{\mathrm{m}}(\mathbf{x})$ are equivalent to the volume fraction of scatterers ϕ_{s} and matrix ϕ_{m} [63,64]:

$$\langle I_{\mathrm{s}}(\boldsymbol{x})\rangle=\phi_{\mathrm{s}}\quad , \tag{6a}$$

$$\langle I_{\mathrm{m}}(\boldsymbol{x})\rangle=\phi_{\mathrm{m}}=1-\phi_{\mathrm{s}}\quad . \tag{6b}$$

The correlation function of material-property fluctuations in the medium is in the following form [65]:

$$R_{ij}(\boldsymbol{r})=\frac{\left|A_i^{(\mathrm{m})}-A_i^{(\mathrm{s})}\right|\left|A_j^{(\mathrm{m})}-A_j^{(\mathrm{s})}\right|}{\langle A_i\rangle\langle A_j\rangle}\left[\langle I_{\mathrm{s}}(\boldsymbol{x}_1)I_{\mathrm{s}}(\boldsymbol{x}_2)\rangle-\phi_{\mathrm{s}}^{2}\right]\quad , \tag{7}$$

where r represents the distance between two locations $\mathbf{x}_1$ and $\mathbf{x}_2$. The parameters $A_i^{(\mathrm{s})}$ and $A_i^{(\mathrm{m})}$ denote magnitudes of material property i (i and j can be density ρ, Lamé second parameter μ and Lamé first parameter λ) of the scatterer and matrix, respectively. The parameter $<A_i>$ represents the average material property, which can be expressed using the following equation:

$$\langle A_i\rangle=\phi_{\mathrm{s}}A_i^{(\mathrm{s})}+\phi_{\mathrm{m}}A_i^{(\mathrm{m})}\quad . \tag{8}$$

The derivation of Equation (7) can be found in Appendix A.

By introducing a normalized correlation function $R(r)$, the second-order statistics of the fluctuations in Equation (7) can be defined as [66,67]:

$$\begin{aligned}\langle I_{\mathrm{s}}(\boldsymbol{x}_1)I_{\mathrm{s}}(\boldsymbol{x}_2)\rangle-\phi_{\mathrm{s}}^{2}&=\phi_{\mathrm{s}}\phi_{\mathrm{m}}R(|\boldsymbol{x}_1-\boldsymbol{x}_2|)\\&=\phi_{\mathrm{s}}\phi_{\mathrm{m}}R(r)\quad .\end{aligned} \tag{9}$$

Substituting Equation (9) into Equation (7) gives:

$$R_{ij}(\boldsymbol{r})=A_{ij}\phi_{\mathrm{s}}\phi_{\mathrm{m}}R(r)\quad , \tag{10a}$$

where A_{ij} is defined as the contrast of the properties for the two phases:

$$A_{ij}:=\frac{\left|A_i^{(\mathrm{m})}-A_i^{(\mathrm{s})}\right|\left|A_j^{(\mathrm{m})}-A_j^{(\mathrm{s})}\right|}{\langle A_i\rangle\langle A_j\rangle}\quad . \tag{10b}$$

An example using density ρ for $A_{\rho\rho}$ is presented in Appendix A. The form for the normalized correlation function $R(r)$ is assumed to be an exponential function, which is able to describe correlations in continuous and discrete materials fairly well [58,68]:

$$R(r)=e^{-\frac{r}{H}}\quad , \tag{11}$$

where H is the characteristic correlation length. In an exponential correlation model of the form shown in Equation (11), the characteristic correlation length H quantifies the spatial scale over which the phase indicator remains correlated. This parameter is usually used to estimate the heterogeneity scale of the material [69–71]. In a binary material with monodisperse and randomly distributed scatterers, the heterogeneity scale is primarily governed by the spatial arrangement of the scatterers. In this setting, the characteristic length H can be interpreted as an effective inter-scatterer spacing [44], because both quantities reflect the typical distance over which the material transitions from one phase to the other.

In the calculation of total scattering cross-sections, the spatial correlation function should be transformed into the Fourier domain. Together with Equations (7), (9) and (11), the PSD or CPSD of material-property fluctuations is given as follows:

$$\widetilde{R}_{ij}(\boldsymbol{k})=\frac{A_{ij}\phi_{\mathrm{s}}\phi_{\mathrm{m}}H^{3}}{\pi^{2}\left(1+H^{2}k^{2}\right)^{2}}\quad , \tag{12}$$

where i and j can be density ρ, Lamé first parameter λ and Lamé second parameter μ. The derivation details for the spatial Fourier transform can be found in Appendix B. Then, Equation (2) can be written as:

$$\begin{aligned}\widetilde{R}_{ij}^{\mathrm{KL}}(\chi) &= \widetilde{R}_{ij}^{\mathrm{KL}}(|\boldsymbol{k}_{\mathrm{K}}-\boldsymbol{k}_{\mathrm{L}}|) \\ &= \frac{A_{ij}\phi_{\mathrm{s}}(1-\phi_{\mathrm{s}})H^3}{\pi^2\left[1+H^2(|\boldsymbol{k}_{\mathrm{K}}-\boldsymbol{k}_{\mathrm{L}}|)^2\right]^2} \\ &= \frac{A_{ij}\phi_{\mathrm{s}}(1-\phi_{\mathrm{s}})H^3}{\pi^2(1+x_{\mathrm{K}}^2+x_{\mathrm{L}}^2-2x_{\mathrm{K}}x_{\mathrm{L}}\chi)^2}\ ,\end{aligned} \tag{13}$$

where x_{K} or x_{L} are dimensionless frequencies defined as $x_{\mathrm{K}}=\omega H/v_{\mathrm{K}}$ or $x_{\mathrm{L}}=\omega H/v_{\mathrm{L}}$. After incorporating possible combinations of wave mode transitions, Equation (13) can be expressed as follows:

$$\widetilde{R}_{ij}^{\mathrm{PP}}(\chi) = \frac{A_{ij}\phi_{\mathrm{s}}(1-\phi_{\mathrm{s}})H^3}{\pi^2[1+2x_{\mathrm{P}}^2(1-\chi)]^2}\ , \tag{14a}$$

$$\widetilde{R}_{ij}^{\mathrm{SS}}(\chi) = \frac{A_{ij}\phi_{\mathrm{s}}(1-\phi_{\mathrm{s}})H^3}{\pi^2\left[1+2x_{\mathrm{S}}^2(1-\chi)\right]^2}\ , \tag{14b}$$

$$\widetilde{R}_{ij}^{\mathrm{PS}}(\chi) = \widetilde{R}_{ij}^{\mathrm{SP}}(\chi) = \frac{A_{ij}\phi_{\mathrm{s}}(1-\phi_{\mathrm{s}})H^3}{\pi^2\left(1+x_{\mathrm{P}}^2+x_{\mathrm{S}}^2-2x_{\mathrm{P}}x_{\mathrm{S}}\chi\right)^2}\ . \tag{14c}$$

As indicated by Equation (14), the key parameters required for evaluating the total scattering cross-sections include the longitudinal and transverse wave velocities (v_{P} and v_{S}), the angular frequency (ω), the characteristic correlation length (H), the volume fraction of scatterers (ϕ_{s}), and the material property contrast between the two phases (A_{ij}). Among the parameters mentioned above, the wave velocities and angular frequency can be acquired from the received signal. In an idealized binary medium composed of monodisperse spherical scatterers, ϕ_{s} and H are not independent. A higher scatterer volume fraction reduces the average spacing between scatterers and therefore yields a shorter correlation length. Under this assumption, once the scatterer volume fraction and diameter are known, the characteristic correlation length follows directly from their geometrical relationship. Determination of ϕ_{s} and H requires first establishing which concrete constituents should be treated as the matrix and which should be regarded as scatterers. This identification forms the basis of the subsequent analysis and is addressed in the next section.

3.2. Matrix and possible scatterers in concrete

As discussed in Section 3.1, the scattering behaviour of body waves in concrete is governed by five parameters: wave velocities, the wave angular frequency, the material-property contrast between the matrix and the scatterers, the scatterer volume fraction, and the characteristic correlation length. Under the idealized representation of concrete as a binary medium with monodisperse spherical scatterers that are uniformly and randomly distributed, the characteristic correlation length becomes a deterministic function of the scatterer diameter and volume fraction. In addition, wave velocities can be directly estimated in experiments, and the angular frequency of the incident wave can be intentionally controlled during measurement. Accounting for these dependencies, the independent material-related parameters reduce to three: the material-property contrast, the scatterer volume fraction, and the scatterer diameter.

Concrete contains several potential scatterers, including air voids, reinforcement, and coarse aggregates. To contribute meaningfully to the scattering process, a phase must exhibit (i) a significant material contrast relative to the matrix, (ii) a non-negligible volume fraction, and (iii) a diameter sufficiently large relative to the wavelength considered. Air voids, despite their strong material contrast, typically have diameters below 3 mm [72], which limits their contribution to scattering for frequencies below 500 kHz, for which the transverse-wave wavelength in concrete is approximately 5.4 mm. Reinforcement has a small volume fraction (e.g., a maximum longitudinal reinforcement ratio of 4% in beams [73]), resulting in a theoretically limited contribution to body wave scattering. For coarse aggregates, scattering may originate either from the aggregates themselves or from the ITZ surrounding them. In ordinary concrete, the ITZ is highly porous and mechanically weaker than the bulk paste [74]. Its thickness, typically less than 0.15 mm [75,76], is much smaller than the coarse aggregate diameter, which is larger than 4 mm. Reported elastic moduli of the ITZ range from 20% to 85% of that of the matrix (as summarized in Table 1). In contrast, in alkali-activated or geopolymer concretes, the elastic modulus of the ITZ can be comparable to or even exceed that of the matrix [77,78].

Table 1
Summary of the material property difference between ITZ and the matrix.

Study	Material	Property contrast between ITZ and matrix		
		Density ratio $\rho_{\mathrm{ITZ}}/\rho_{\mathrm{matrix}}$	Poisson's ratio $\upsilon_{\mathrm{ITZ}}/\upsilon_{\mathrm{matrix}}$	Elastic modulus $E_{\mathrm{ITZ}}/E_{\mathrm{matrix}}$
[79]	Cement mortar	–*	1	0.6
[80]	Concrete	–	1.2	0.5
[81]	Concrete	–	–	0.7 to 0.85
[82]	Concrete	–	1	0.404 and 0.384
[83]	Concrete	–	1	0.509
[84]	Concrete	–	1.2	0.477
[76]	Concrete	–	–	From 0.2 to 0.8
[85]	Geopolymer	–	–	1.015
[86]	Geopolymer	–	–	0.974 and 1.205

Note: "-" indicates that this information is not provided in the paper.

Based on these considerations, the ITZ surrounding coarse aggregates is a highly probable source of scattering for body waves in ordinary concrete, as also emphasised by Ramaniraka et al. [34,35]. In concrete systems with a mechanically strong ITZ, such as geopolymer concretes, the dominant scattering source is more likely to be the coarse aggregates themselves. In the following calculation, the heterogeneous medium is consistently represented by a two-phase configuration. Depending on the focus of the analysis, either the coarse aggregates or the ITZs are treated as the effective scattering phase embedded in a homogeneous matrix. When the ITZ is considered as the scatterer, its response is modelled as an effective interfacial heterogeneity, and the internal structure of the coarse aggregate core is not explicitly resolved. Explicitly resolving the matrix, aggregate, and ITZ as three distinct phases would significantly increase model complexity and is therefore typically treated using numerical simulation approaches in the literature [34,35].

3.3. Determination of parameters in the analytical framework using concrete characteristics

In the previous two sections, we have discussed the PSD/CPSD of the simplified two-phase concrete as well as possible scatterers in concrete. We have identified key parameters required for evaluating the total scattering cross-sections, including the longitudinal and transverse wave velocities, the angular frequency, the characteristic correlation length, the volume fraction of scatterers, and the material property contrast between the two phases. Among them, the characteristic correlation length and the volume fraction of scatterers are correlated under the current assumptions (a binary material containing monodisperse, spherical scatterers that are uniformly and randomly distributed in space) and therefore must be reformulated into independent, determinable variables. In addition, further simplifications are required to assign reasonable values to the material-property contrast between the two phases, which is otherwise difficult to quantify.

Following the approach commonly used in snow and random-media scattering [87,88], where the exponential correlation length is parameterised in terms of an effective grain size and the volume fraction, we adopt a simplified geometrical model in which the characteristic spacing

H is expressed as a function of the scatterer characteristic radius r_s and volume fraction ϕ_s. This is consistent with the general practice of relating microstructural length scales to inclusion size and volume fraction in two-phase random media, although the specific form should be viewed as a model choice tailored to the present sphere idealisation rather than a universal result. This transformation converts the correlated pair (H,ϕ_s) into two independent and directly controllable inputs (r_s,ϕ_s). Assuming that all scatterers are monodisperse spheres of radius r_s uniformly and randomly distributed in space, consider a differential slab of area A [m^2] and thickness dx [m]. The total number of scatterers in this element is $\phi_s A\mathrm{d}x/(4/3 \times \pi r_s^3)$. The total area blocked by these scatterers is therefore:

$$\begin{aligned} \mathrm{d}A &= -\frac{\phi_s A\mathrm{d}x}{\frac{4}{3}\pi r_s^3}\pi r_s^2 \\ &= -\frac{3\phi_s}{4r_s}A\mathrm{d}x \ . \end{aligned} \tag{15}$$

The derivation in Equation (15) appears to involve only the volume fraction and scatterer characteristic radius, but it actually originates from the projected area πr_s^2 of each spherical scatterer. When the number density ($\phi_s A\mathrm{d}x$ divided by the sphere volume) is multiplied by the projected area, the geometric constants cancel, which yields a final expression that no longer contains an explicit area term. The resulting differential equation has the form of an exponential decay, and its associated decay length defines the correlation length:

$$H = \frac{4r_s}{3\phi_s} \ . \tag{16}$$

Although the mathematical form of Equation (16) resembles the exponential attenuation used to define a mean free path [89], the physical meanings differ fundamentally. The characteristic correlation length H arises purely from the spatial statistics of the phase distribution and does not describe the decay of wave amplitude or energy.

As noted in Section 3.2, the ITZ is a likely scattering source in ordinary concrete, while in materials with a stronger ITZ the coarse aggregates dominate instead. Considering that the ITZ forms only a thin shell, the characteristic radius of scatterers is effectively determined by the characteristic radius of coarse aggregates in either case. Estimating this aggregate radius requires a scatterer-size distribution. The characteristic radius is computed using the following expression [90]:

$$\frac{4}{3}\pi r_s^3 = \frac{V}{\int_{r_{\min}}^{r_{\max}} \frac{v(r_c)}{\frac{4}{3}\pi r_c^3}\mathrm{d}r_c} \ , \tag{17a}$$

where V represents the total volume of coarse aggregates, r_c is the characteristic radius for monodisperse spherical scatterers, and $v(r_c)$ is the volume associated with aggregates of radius r_c. The true aggregate size distribution is continuous, and Equation (17a) follows this continuous representation. To provide an engineering estimate of the underlying continuous scatterer diameter distribution, the discrete form of Equation (17a) is adopted to approximate this continuous distribution using sieve-based grading intervals, leading to the discrete approximation:

$$r_s = \left(\sum_{i=1}^{g}\frac{n_i}{r_i^3}\right)^{-\frac{1}{3}} \ . \tag{17b}$$

where n_i denotes the volume ratio within the grading interval i, and r_i is the characteristic radius within this grading interval.

In computing the PSD and CPSD of material-property fluctuations, the contrast factor A_{ij} acts as a multiplicative amplitude term that depends on the absolute contrasts in density ρ, the Lamé first parameter λ, and the Lamé second parameter μ. Obtaining these absolute contrasts at the microscale is challenging in practice: all three quantities would need to be measured locally within the ITZ and coarse aggregates to define not only the PSDs but also the CPSDs between ρ, λ and μ. Such measurements are rarely achievable experimentally. Moreover, even the available microscale elastic modulus data exhibit substantial variability, as shown in Table 1, and no corresponding microscale density data have been reported. Because a numerical implementation based on full PSD/CPSD information would be intractable without these unavailable microscale contrasts, the contrast factor A_{ij} is then normalized to 1 in the PSD/CPSD formulation. This simplification preserves the spatial statistics of the fluctuations while making the framework practically applicable. The physical interpretation and the conditions under which the simplification $A_{ij} = 1$ remains valid are discussed in Section 5.1. The resulting expressions for the total and transport cross-sections of concrete are provided in Appendix C.

4. Validation of total scattering cross-sections using concrete specimens

This section presents the experimental validation of the proposed scattering framework. Ultrasonic measurements were performed on geopolymer concrete beams and slabs to obtain frequency-dependent diffusivities, which are directly compared with theoretical predictions, and the applicability of the framework to ordinary concrete is further assessed by comparison with published experimental diffusivity data.

4.1. Validation using geopolymer concrete beams

The experimental validation of total scattering cross-sections involves three geopolymer concrete members: two beams and one slab. The geometry, sensor layout, and the experimental details of the geopolymer concrete members are introduced in Appendix D.

The governing equation for diffusion can be written in the following form [41,91]:

$$\frac{\partial E(\boldsymbol{x},t)}{\partial t} = D\nabla^2 E(\boldsymbol{x},t) - \sigma E(\boldsymbol{x},t) + E_0\delta(\boldsymbol{x}-\boldsymbol{x}_0)\delta(t) \ , \tag{18}$$

where t represents the time and $\mathbf{x}$ is the spatial vector. $E(\mathbf{x},t)$ is the transport energy at location $\mathbf{x}$ and time t, and E_0 represents the deposited impulse energy at the initial location at time $t = 0$ [41]. The parameters D and σ represent the diffusivity and dissipation, respectively, that describe the characteristics of energy transport. To simplify the formulation, the cross sections shown in Figs. D2(a), D3(a), and D4(a) are approximated as rectangular. As illustrated in the figures, only small, localized regions near the lower corners of the cross sections are not occupied by concrete. The area of these regions accounts for approximately 1.8% of the total rectangular cross-sectional area in the beam case and 1.2% in the slab case. Given their limited extent, approximating the cross sections as rectangular is considered a sufficiently accurate assumption for the purposes of this analysis. For a cuboid three-dimensional medium, the solution of Equation (18) is given as [22,26,92]:

$$\begin{aligned} E(\boldsymbol{a}_S,\boldsymbol{a}_R,t) = E_0 e^{-\sigma t} \times & \left[1+2\sum_{n=1}^{\infty}\cos\left(\frac{n\pi x_S}{L_S}\right)\cos\left(\frac{n\pi x_R}{L_S}\right)e^{-D\left(\frac{n\pi}{L}\right)^2 t}\right] \\ & \times \left[1+2\sum_{n=1}^{\infty}\cos\left(\frac{n\pi y_S}{H_S}\right)\cos\left(\frac{n\pi y_R}{H_S}\right)e^{-D\left(\frac{n\pi}{L}\right)^2 t}\right] \\ & \times \left[1+2\sum_{n=1}^{\infty}\cos\left(\frac{n\pi z_S}{W_S}\right)\cos\left(\frac{n\pi z_R}{W_S}\right)e^{-D\left(\frac{n\pi}{L}\right)^2 t}\right] \ , \end{aligned} \tag{19}$$

where $\mathbf{a}_S$ and $\mathbf{a}_R$ denote the position vectors of the source and receiver, with coordinates (x_S,y_S,z_S) and (x_R,y_R,z_R), respectively, defined with respect to the coordinate system shown in Appendix D. The parameters L_S, H_S, and W_S represent the length, height, and width of the concrete

beam or slab. For the configurations illustrated in Figs. D2 and D3, L_S, H_S, and W_S are set to 7.35, 0.42, and 1.10, respectively. For the configuration shown in Fig. D4, L_S, H_S, and W_S are taken as 7.35, 0.42, and 3.19, respectively. The logarithmic form of Equation (19) is employed in fitting the diffusivity and dissipation.

The diffusivity was estimated from the experimental results through the following steps:

- **CWT-based frequency decomposition**: The recorded signals are first decomposed into frequency-dependent energy using the squared modulus of the continuous wavelet transform (CWT) coefficients with the analytical Morlet wavelet. The full analysed frequency range is 50 Hz to 1 MHz (the sampling rate is 3 MHz), with 10 voices per octave. For the experimental diffusivity analysis, the selected frequencies range from 50 kHz to 400 kHz with a 50 kHz interval. For the 50, 100, 150, and 200 kHz bands, the energy is obtained by averaging the CWT coefficients at the central frequency and the two adjacent frequency scales, whereas for the 250, 300, 350, and 400 kHz bands, only the central-frequency scale is used because the corresponding CWT bands were already sufficiently broad.
- **Time-windowed ensemble averaging**: The energy at each frequency is then ensemble-averaged within a sequence of overlapping time windows. The first 11 windows have a duration of 40 μs, starting from 25 μs, with 20 μs overlap between consecutive windows. From the 12th window onward, the window length is increased to 100 μs, starting at 225 μs, and the subsequent 10 windows overlap by 50 μs.
- **Least-squares diffusivity fitting**: The logarithm of the resulting windowed, time-dependent energy is fitted to estimate the best-fit diffusivity D, dissipation σ, and initial deposited energy E_0 through unweighted least-squares minimization of the discrepancy between the measured and modelled logarithmic energy evolution. The spread of the extracted diffusivity values across different members and sensor locations is represented using boxplots. This provides a practical characterization of variability, although it should be distinguished from a rigorous uncertainty propagation analysis.

The dry density of coarse aggregates used in concrete members is 2630 kg/m^3. The volume fraction of coarse aggregates in the concrete can be directly deduced from the mixture composition, as shown in Table 2. The volume fraction of coarse aggregates is 25.7%. The characteristic radius of coarse aggregates is computed using Equation (17b), and the sieving of coarse aggregates is provided in Table 3. Within each grading interval, there are two characteristic radii: the maximum radius and the minimum radius, which are related to the range of particle sizes that can be effectively separated. To explore the impact of the choice of the characteristic radii on diffusivities predicted by the theoretical framework, both the maximum and minimum radii within grading intervals are employed as the characteristic radii of coarse aggregates in the respective calculations. The estimated characteristic maximum and minimum radii of coarse aggregates are 4.45 mm and 3.12 mm, respectively. Accordingly, the corresponding characteristic correlation lengths H are 23.07 mm and 16.18 mm, respectively. The average longitudinal wave velocity measured in geopolymer concrete members is 4544 m/s. The average transverse wave velocity, which is estimated using a factor of 0.61 [93], is 2772 m/s.

Table 2
Mixture composition of the geopolymer concrete.

Materials	Content (kg/m^3)
Blast furnace slag	550.0
NaOH solution (50.0 wt%)	36.9
Sodium silicate solution (48.0 wt%)	80.4
Water	191.0
Admixture/Retarder	1.375
Sand: 0–4 mm	762.0
Gravel: 4–16 mm	676.0

Table 3
Sieving of coarse aggregates in the geopolymer concrete.

Coarse aggregates diameter	12–16 mm	8–12 mm	5.6–8 mm	4–5.6 mm
Volume ratio	22.6%	38.9%	28.1%	10.4%

Fig. 1 illustrates how the experimental diffusivities compare with the theoretical predictions obtained by assigning the minimum and maximum aggregate radii within each grading interval as the characteristic radius. The two theoretical curves remain close throughout the frequency range, indicating that the scatterer-size ambiguity introduced by the grading-interval discretization produces only a limited spread in the predicted response. To quantify the agreement between theoretical and experimental diffusivities, Table 4 reports the experimental median value, mean value ± standard deviation, 95% confidence interval, relative error, standardized error, and MAPE at each frequency. In the low-frequency regime (50–150 kHz), the experimental diffusivities show substantial dispersion, and although the theoretical predictions remain within the overall experimental variability, they deviate slightly from the measurements. This is particularly evident at 100 kHz, where the relative error reaches 31.39%. One plausible reason is the use of a monodisperse scatterer idealization across all frequency components. When the low- and high-frequency bands are considered separately, the inferred characteristic radii may differ. This suggests that different frequencies preferentially sample different parts of the scatterer size distribution, an effect that the current idealization cannot fully capture.

At higher frequencies (200–400 kHz), the theoretical predictions remain reasonably consistent with the experimental results, although they are systematically lower than the experimental means. As shown in Table 4, the relative errors in this range are between 15.33% and 25.17%, while the standardized errors range from 0.860 to 1.425, indicating that the deviations remain comparable to the intrinsic scatter of the experimental diffusivity data. This quantitative comparison indicates that the framework captures the overall frequency dependence and order of magnitude of diffusivity in geopolymer concrete, which further suggests that the proposed analytical framework successfully reproduces the frequency-dependent scattering induced by the contrast between coarse aggregates and matrix in geopolymer concrete. Additionally, this observation reinforces the validity of the simplifying assumptions adopted in the derivation, including the use of a characteristic scatterer radius and the normalization of material-contrast factors. Despite these simplifications, the model reproduces experimental observations with satisfactory accuracy, indicating that the essential mechanisms of multiple scattering in concrete have been appropriately incorporated.

4.2. Validation using concrete prism reported by Anugonda et al. [44]

To examine the applicability of the proposed analytical framework to ordinary concrete, we further test the framework using diffusivity data reported by Anugonda et al. [44]. It should be noted that diffusivity measurements for ordinary concrete were also reported by Ahn et al. [94,95]. However, their measurements were obtained using surface-based sensors and therefore likely reflect a combined effect of body-wave and surface-wave diffusivity. Because the present framework is primarily based on body waves, such data cannot be directly utilized here.

In the experiment reported by Anugonda et al. [44], the frequency ranges from 100 kHz to 900 kHz with a 100 kHz interval. The volume fraction of coarse aggregates used in their calculation is 58.8%. However, this value did not account for the contribution of water. In their paper, the water-cement ratio is 0.5 and the volume ratio of cement/sand/coarse aggregates is 1:2.5:5. Considering the absolute density of cement around 3.1 g/cm^3 [96], the volume ratio of water/cement/sand/

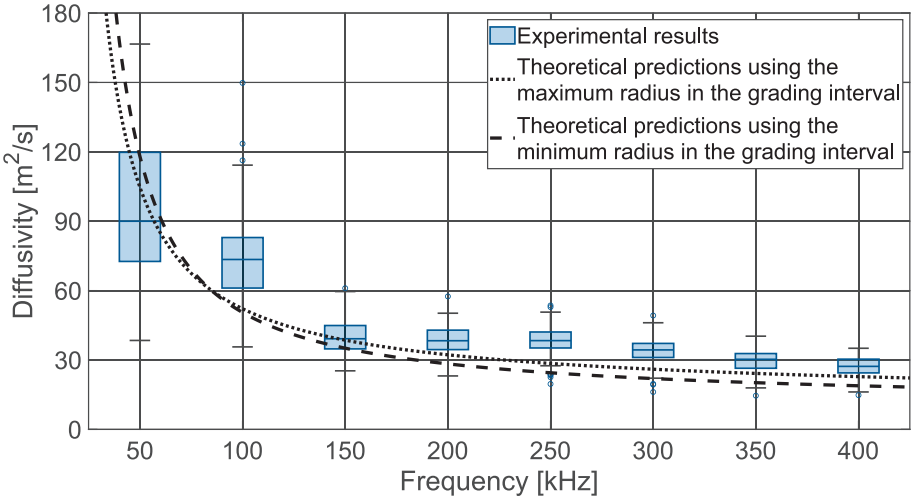

Fig. 1. Validation of total scattering cross-section by means of diffusivities from experiments. The box plot is employed to visually demonstrate the spread of diffusive properties measured in the experiment. The box spans the first and third quartiles (Q1 and Q3), the line inside the box marks the median, and the whiskers extend to the most extreme non-outlier values within 1.5 interquartile range (IQR) of Q1 and Q3. Outliers, depicted as circles, are values that exceed 1.5 times IQR above or below the top or bottom of the box.

Table 4
Comparison between theoretical and experimental diffusivities at different frequencies, with corresponding error metrics.

Frequency [kHz]	Theoretical diffusivity [m[b]/s]	Experimental diffusivity [m[b]/s]			Evaluation between theoretical and experimental diffusivities		
		D_{median}	$D_{mean} \pm D_{std}$	95% confidence interval[a]	Relative error[b]	Standardized error[c]	MAPE[d]
50	104.73	90.00	106.22 ± 60.18	[92.47,119.97]	1.40%	0.025	36.12%
100	52.17	73.46	76.04 ± 22.52	[70.89,81.19]	31.39%	1.060	29.35%
150	38.58	39.18	39.99 ± 8.03	[38.16,41.83]	3.53%	0.176	15.92%
200	32.25	38.33	38.11 ± 6.82	[36.55,39.67]	15.38%	0.860	19.00%
250	28.51	38.38	38.10 ± 6.73	[36.56,39.64]	25.17%	1.425	25.99%
300	26.01	34.36	33.64 ± 6.20	[32.22,35.05]	22.68%	1.230	24.62%
350	24.20	30.30	29.51 ± 5.23	[28.31,30.70]	17.99%	1.016	21.32%
400	22.81	27.24	26.94 ± 4.75	[25.85,28.02]	15.33%	0.869	19.58%

[a] Calculated using the equation: $D_{mean} \pm 1.992 \times D_{std}/\mathrm{sqrt}(N_{sample})$, where N_{sample} represents the total number of samples and is equal to 76.
[b] Relative error (RE) is calculated using the equation: $|D_{theoretical}\text{-}D_{mean}|/D_{mean}$.
[c] Standardized error (SE) is calculated using the equation: $|D_{theoretical}\text{-}D_{mean}|/D_{std}$.
[d] Mean absolute percentage error (MAPE) is calculated using the equation: $100 \times \mathrm{sum}(|D_{theoretical}\text{-}D_{experimental}|/D_{experimental})/N_{sample}$.

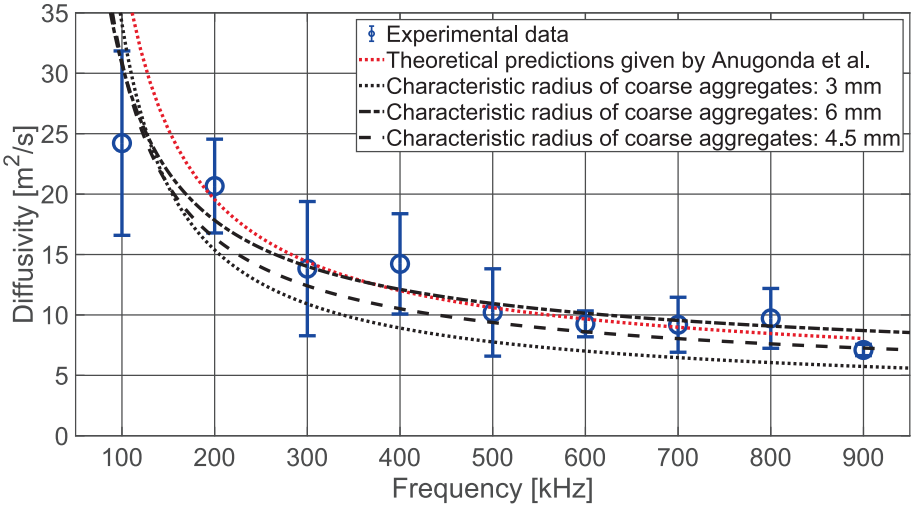

Fig. 2. Validation of the proposed framework's applicability to ordinary concrete using data from Anugonda et al. [44].

coarse aggregates is 1.55:1:2.5:5. Therefore, a more accurate volume ratio of coarse aggregates including water is around 49.75%, slightly lower than the original value. The average longitudinal and transverse wave velocities reported are 4240 m/s and 2450 m/s, respectively. Since only the maximum coarse aggregate size, 12.7 mm, was mentioned in the paper and no further information was provided, we considered three characteristic coarse-aggregate radii, 3 mm, 4.5 mm, and 6 mm in the calculation, which correspond to characteristic correlation lengths H of

Table 5
Comparison of experimental mean diffusivity and theoretical diffusivity under different parameter settings.

Frequency [kHz]	Mean diffusivity acquired from the experiment [m^2/s]	Theoretical diffusivity [m^2/s] Theoretical predictions by Anugonda et al. [44]	r_s = 3 mm (volume ratio 49.75%)	r_s = 4.5 mm (volume ratio 49.75%)	r_s = 6 mm (volume ratio 49.75%)	r_s = 6 mm (volume ratio 58.8%)
100	24.22	39.58	34.11	30.95	30.76	31.67
200	20.67	19.54	15.39	16.37	17.83	17.45
300	13.83	14.40	10.92	12.41	14.02	13.44
400	14.23	12.01	8.92	10.51	12.12	11.49
500	10.21	10.60	7.77	9.38	10.96	10.31
600	9.26	9.66	7.01	8.60	10.14	9.50
700	9.19	8.98	6.48	8.04	9.56	8.90
800	9.72	8.46	6.06	7.61	9.09	8.44
900	7.10	8.05	5.74	7.26	8.71	8.07
Mean relative error between theoretical and experimental results across frequencies		13.93%	28.81%	15.19%	11.88%	11.33%

8.04 mm, 12.06 mm and 16.08 mm, respectively.

Fig. 2 presents a comparison between the experimentally measured diffusivities and the theoretical predictions obtained using three different characteristic radii for the coarse aggregates (3 mm, 4.5 mm, and 6 mm). To quantify this comparison, Table 5 summarizes the theoretical diffusivities obtained for the three assumed characteristic radii and reports the mean relative error between theoretical and experimental diffusivities across the investigated frequency range. As shown in Table 5, the mean relative error decreases from 28.81% for r_s = 3 mm to 15.19% for r_s = 4.5 mm and further to 11.88% for r_s = 6 mm. The experimental data fall predominantly within this radius-induced envelope, especially in the intermediate- and high-frequency ranges (300–900 kHz). This alignment implies that these estimated characteristic radii are consistent with the microstructural scale that governs ultrasonic scattering. At lower frequencies (100–200 kHz), the theoretical predictions deviate from experimental diffusivities. This discrepancy may also stem from the monodisperse scatterer idealization discussed in Section 4.1. Nonetheless, the deviation remains moderate, and the experimental uncertainty still brackets theoretical predictions. Table 5 also shows that changing the coarse-aggregate volume ratio from the recalculated value of 49.75% to the originally reported value of 58.8% for r_s = 6 mm changes the mean relative error only slightly, from 11.88% to 11.33%. This indicates that the influence of the volume fraction is noticeable but not substantial. The overall level of agreement confirms that the essential scattering mechanisms have been captured by the analytical framework, including the matrix-ITZ contrast and the choice of characteristic scatterer size. Overall, this consistency suggests that the framework is capable of describing wave diffusion in ordinary concrete, where the ITZ serves as the main source of scattering events, reinforcing the validity of the underlying assumptions and approximations employed in the analytical framework.

5. Discussion

5.1. Simplification of material property contrast

In Section 3.2, the contrast factor A_{ij} in the PSD/CPSD formulation is normalized to unity. Although this normalization is introduced for calculation convenience, it implicitly corresponds to an effective level of material-property contrast between scatterers and the matrix. To clarify the physical scale represented by this normalization, the resulting implied contrasts in different material systems are examined below.

For geopolymer concrete, where the ITZ may be comparable to or stronger than the matrix, the coarse aggregates act as the dominant scatterers. Under the normalization $A_{ij} = 1$, the implied contrast $A_i^{(s)}/A_i^{(m)} = 2.346$ leads to an elastic modulus ratio $E^{(s)}/E^{(m)} = 2.346$, consistent with reported nanoindentation values of approximately 2.5 [86]. The corresponding Poisson's ratio contrast, $\upsilon^{(s)}/\upsilon^{(m)} = 1$, is difficult to assess because data on geopolymer mortar are limited. By contrast, the density contrast, $\rho^{(s)}/\rho^{(m)} = 2.346$, is likely overestimated, because existing studies [97,98] suggest that coarse aggregates are only slightly denser than geopolymer mortar. For ordinary concrete, where the ITZ is weaker than the paste matrix, the ITZ is the primary scatterer. In this case, $A_{ij} = 1$ corresponds to $A_i^{(s)}/A_i^{(m)} = 0.332$. The resulting elastic modulus ratio $E^{(s)}/E^{(m)} = 0.332$ and Poisson's ratio $\upsilon^{(s)}/\upsilon^{(m)} = 1$ are broadly consistent with the values summarized in Table 1. The implied density ratio $\rho^{(s)}/\rho^{(m)} = 0.332$ cannot be evaluated because the density of the ITZ is difficult to directly measure through experiments. While these implied contrasts help interpret the physical meaning of the normalization, they do not by themselves show how strongly the model predictions depend on the adopted value of A_{ij}.

To complement the above physical interpretation, a dedicated sensitivity analysis was performed by varying A_{ij} from 0.50 to 1.50 for the two validation cases considered in this study. The resulting predicted diffusivities are shown in Fig. 3, with representative numerical values summarized in Table 6. A clearer pattern emerges from these results: for both geopolymer and ordinary concrete, varying A_{ij} from 0.50 to 1.50 produces a systematic shift in the predicted diffusivity over their respective investigated frequency ranges. Relative to the baseline case

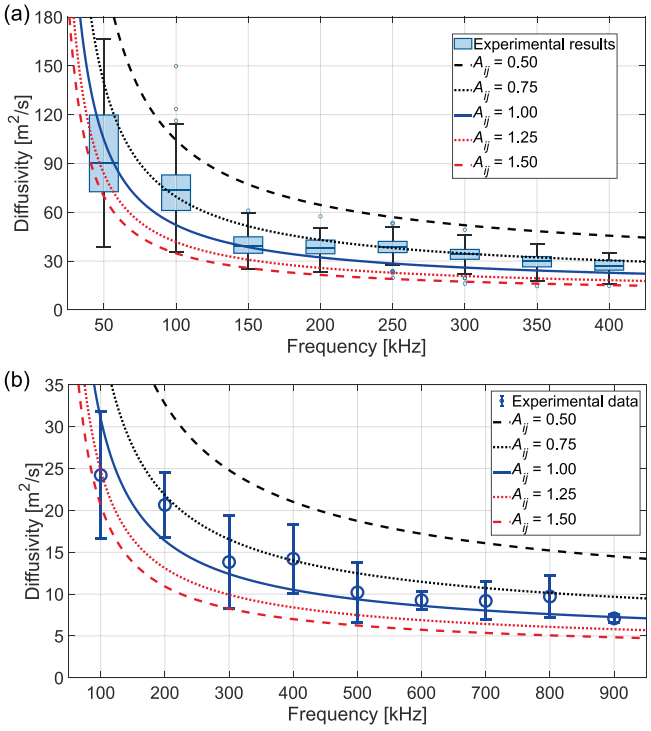

Fig. 3. Sensitivity of the predicted diffusivity to A_{ij} for geopolymer concrete and ordinary concrete. (a) Geopolymer concrete. Theoretical values are calculated using the maximum radius within the grading interval. (b) Ordinary concrete. Theoretical values are calculated assuming r_s=4.5 mm.

Table 6
Predicted diffusivities at selected frequencies for geopolymer and ordinary concrete under different A_{ij} values.

		Diffusivity [m^2/s] $A_{ij} = 0.50$	$A_{ij} = 0.75$	$A_{ij} = 1.00$	$A_{ij} = 1.25$	$A_{ij} = 1.50$
Geopolymer concrete	50 kHz	209.45	139.63	104.73	83.78	69.82
	200 kHz	64.50	43.00	32.25	25.80	21.50
	300 kHz	52.02	34.68	26.00	20.81	17.34
	400 kHz	45.62	30.41	22.21	18.25	15.21
Ordinary concrete	100 kHz	65.59	43.73	32.79	26.24	21.86
	400 kHz	20.16	13.44	10.08	8.06	6.72
	600 kHz	16.25	10.83	8.13	6.50	5.42
	900 kHz	13.55	9.04	6.78	5.42	4.52

$A_{ij} = 1$, the predicted diffusivity varies in inverse proportion to A_{ij} across the considered frequencies, indicating that A_{ij} primarily acts as an effective scaling factor in the model. This is because, in the present formulation, the same normalized value of A_{ij} is assigned to the contrast terms associated with density and the two Lamé parameters, so that A_{ij} enters the PSD/CPSD expressions as a common multiplicative prefactor rather than as a set of independently varying physical contrasts. Consequently, changing A_{ij} mainly rescales the overall scattering strength and the resulting diffusivity level, while leaving the frequency dependence of the predicted curves essentially unchanged.

Taken together, these observations highlight that the implicit contrasts from $A_{ij} = 1$ should be viewed as an effective measure of scatterer-matrix mismatch rather than as physically exact ratios for each elastic or density parameter. The modulus contrasts produced by the normalization lie within realistic ranges for both geopolymer and ordinary concrete, whereas the Poisson's ratio and density contrasts should not be overinterpreted due to the limited direct experimental access to exact values. More importantly, the analytical framework already incorporates idealized assumptions, i.e., monodisperse spherical scatterers, that oversimplify the true heterogeneity of concrete. Within such an approximation, the purpose of normalizing A_{ij} is not to recover exact contrasts for individual material parameters, but to capture the effective scattering strength associated with the dominant heterogeneities. The close agreement between theoretical and experimentally measured diffusivities therefore suggests that, although the predicted diffusivity is sensitive to the adopted value of A_{ij}, the baseline choice $A_{ij} = 1$ provides a reasonable effective baseline approximation for the two concrete systems considered here.

Viewed from this perspective, the framework is best interpreted as a tool for quantifying the effective scattering contribution of key microstructural phases rather than as a means of assigning detailed physical values to each parameter. This perspective also provides a foundation for extending the framework toward the evaluation of ITZ property changes in ordinary concrete. As discussed earlier, body-wave scattering in the several-hundred-kilohertz range is strongly influenced by the ITZ surrounding coarse aggregates in ordinary concrete. However, current experimental characterizations, primarily nanoindentation [99,100], are usually destructive and provide only localized measurements with substantial variability, ranging from 20% to 85% of the matrix modulus, as shown in Table 1. In contrast, elastic body waves probe a three-dimensional region at the meter scale, and their total scattering cross-sections integrate the response of the ITZ over a much larger volume. Our future work will therefore focus on using the proposed framework to infer statistically effective ITZ property contrasts by fitting directly to experimentally determined diffusivity, rather than assuming $A_{ij} = 1$. It should be emphasized that the objective here is not to extract absolute material properties of the ITZ, which is not realistic within the scope of the proposed framework as discussed above. The intention instead is to retrieve effective ITZ property contrasts from diffuse wave measurements and to use these contrasts as quantitative indicators of relative changes in ITZ properties during damage processes, such as thermal degradation. This capability is particularly important because the evolution of ITZ properties cannot be monitored non-destructively using existing experimental characterization techniques, which are typically localized and often destructive.

5.2. Revisiting the assumptions in the derivation of total scattering cross-sections

The derivation of total scattering cross-sections in Equation (1) is based on three assumptions [46,47]:

1. the medium is statistically isotropic and statistically homogeneous;
2. the phase velocity remains unchanged during the scattering;
3. spatial fluctuations of heterogeneities are weak.

Assumption 1 implies that heterogeneities in the medium are uniformly distributed. This assumption is expected to be reasonable for geophysical materials and concrete [46]. Assumption 2 is the Born approximation [101]. It assumes that scattering events change only the propagation direction and wave mode, while the phase velocities of longitudinal and transverse waves remain constant. This simplification allows expressing the scattered field as a sum of scattered waves emitted by each individual scatterer [13]. By adopting the Born approximation, the scattered amplitude can be directly calculated using the three-dimensional Fourier transform of the potential energy function, with respect to the difference between the incident and scattered wave vectors [102]. In the context of elastic wave scattering in statistically isotropic and statistically homogeneous solids, the potential energy function relates to spatial fluctuations of Lamé constants, λ and μ, as well as density, ρ [47], which govern the propagation of elastic waves in these media. The use of the Born approximation also explains the power spectral densities involved in the expressions shown in Equation (1): the spatial fluctuations are transformed into the power spectral densities in the Fourier domain when applying the Born approximation [47].

The applicability of the Born approximation is determined by the relationship between the wavenumber k and the characteristic diameter of scatterers d_s. This approximation fails when the wavelength is much smaller than the diameter of scatterers [42]. In other words, in the Rayleigh regime [103], where kd_s is smaller than one, or in the Rayleigh-Gans regime [13], where kd_s is of the same order of magnitude as 1, the Born approximation is valid based on previous research [101]. Calvet and Margerin [57,104] indicated that the Born-approximation-based predictions remain reliable up to kd_s of the order of 10. Therefore, $kd_s < 10$ is adopted here as a pragmatic upper bound rather than a rigorous threshold for the applicability of the Born approximation. Fig. 4 shows the relationship between frequency and coarse aggregate diameter at $kd_s = 10$ for longitudinal and transverse waves in ordinary and geopolymer concrete. For geopolymer concrete, the d_s estimated using the maximum radius in the grading interval is 8.90 mm, and the corresponding $k_S d_s$ and $k_P d_s$ at 400 kHz (the maximum frequency for geopolymer concrete investigated in this paper) are 4.93 and 8.07, respectively, both of which are smaller than 10.

For ordinary concrete, the d_s is taken as 9.00 mm, and the corresponding $k_S d_s$ for transverse waves at 500 kHz, 700 kHz, and 900 kHz are 11.54, 16.16, and 20.77, respectively. These values all exceed the

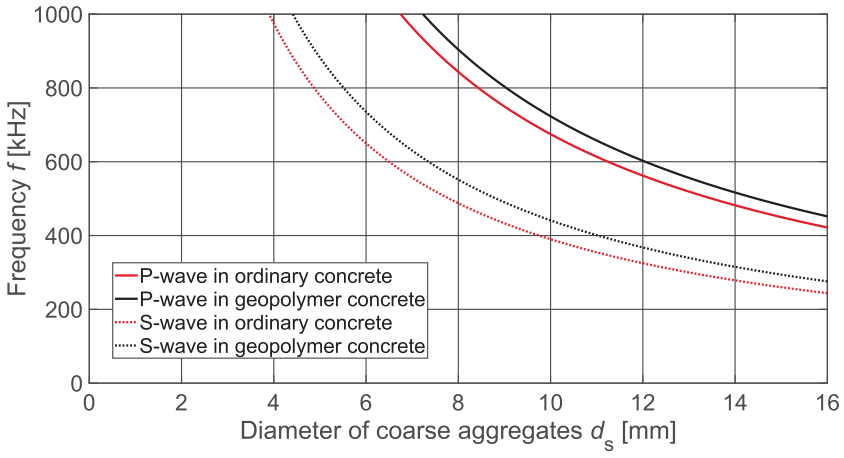

Fig. 4. Relationship between frequency and coarse aggregate diameter corresponding to $kd_s = 10$ for P- and S-waves in ordinary and geopolymer concrete. Regions above each curve satisfy $kd_s > 10$, whereas regions below each curve satisfy $kd_s < 10$.

pragmatic upper bound $k_S d_s < 10$ adopted here. Therefore, the present Born-approximation-based treatment is expected to be on firmer theoretical ground below about 400 kHz, whereas its application at higher frequencies should be interpreted with caution. Nevertheless, the theoretical predictions remain in good agreement with the experimental diffusivities above 400 kHz, as shown in Fig. 2. A possible explanation for this observation is that the quantity compared in this study is transport-level observable, namely diffusivity, which is primarily controlled by ensemble-averaged energy redistribution rather than by the detailed phase evolution of individual scattering events. While the Born approximation may fail to accurately describe the phase and amplitude of single scattering events in the geometrical regime, its use within a multiple scattering framework may still provide approximate predictions for macroscopic energy transport when strong randomness, mode conversion, and repeated scattering act to rapidly erase directional and phase memory. In such cases, geometrical-regime features associated with individual scatterers may be effectively averaged out at the transport scale.

Assumption 3 is intended to avoid the occurrence of localization [48,105,106], a phenomenon in which energy propagation is hindered within a confined region due to significant interference from scatterers. Given the inherent challenge in directly evaluating the existence of localization of body waves in concrete through experiments, which requires the measurement of the multiple backscattering effect [48], the validity of this assumption in concrete should be further checked in future work.

5.3. Possible approaches to improve the performance of the theoretical framework

As discussed in previous sections, the theoretical framework relies on several simplifying assumptions that may influence its performance. Two possible approaches for improving its agreement with experimental data are outlined below.

The first approach focuses on enhancing the normalized correlation function. In this paper, we assume that the normalized correlation function $R(r)$ follows an exponential form. However, this assumption may not hold for the two-phase concrete considered here. To obtain a more accurate estimation of the correlation function, a numerical model specific to concrete is required. See the article published by Liu and Turner [65] for further details.

The second approach therefore involves improving the framework by incorporating a more realistic, multi-scale description of scatterers rather than adopting a monodisperse scatterer idealization. The discrepancy between low- and high-frequency predictions might arise from the fact that the present framework represents the coarse aggregates by a single characteristic scatterer size. Concrete contains a broad and continuous coarse aggregate size distribution, and different frequency components preferentially interact with different parts of this distribution. As a result, a single effective radius cannot reproduce the scattering behaviour consistently across the full frequency range. Allowing the characteristic radius to vary with frequency might not resolve this issue in a physically meaningful way. The scatterer size is a geometric property of the material and should remain independent of frequency; adjusting it for different bands would turn it into a frequency-dependent fitting parameter and introduce strong subjectivity in how the frequency ranges are selected, undermining the predictive nature of the framework. A consistent representation of both low- and high-frequency behaviour would therefore require extending the current formulation to account for a polydisperse or multi-scale population of scatterers. Such an extension would enable different parts of the coarse aggregate size distribution to contribute appropriately to scattering at different frequencies.

5.4. Potential application of the proposed framework to energy equilibration of body waves in concrete

Beyond predicting the scattering and diffusion properties of body waves in concrete, the proposed multiple-scattering framework may also enable the estimation of the energy equilibration process of body waves in concrete. Because the formulation explicitly accounts for possible mode conversions during scattering, it can be incorporated into wave-energy transport models to predict both the equilibration time and the equilibrated energy ratio of body waves in concrete. The equilibration time serves as a key indicator of when the diffusion equation becomes valid for modelling wave-energy transport [47], which is essential for diffusion-based sensitivity-kernel imaging using coda waves [36,38,107–110]. As highlighted by Seher et al. [111], to the best of our knowledge, no widely adopted model is currently available for predicting this equilibration time in concrete. It is also worth noting that sensitivity kernels can be constructed through the radiative transfer equation [112], in which the mean free path is a key input parameter that can be directly obtained from the present framework. The equilibrated energy ratio derived from the framework can be further used to interpret stress-induced velocity changes retrieved from coda waves, which represent an energy-weighted combination of longitudinal and shear velocity changes. A more complete understanding of this weighting mechanism can help link measured coda-wave velocity changes to underlying stress changes, even when only sparse sensing layouts are available [21]. These potential applications suggest that the proposed framework may contribute to future developments in coda-wave-based SHM, and we intend to pursue this direction in subsequent work.

Table 7
Summary of the main assumptions and simplifications, together with their applicability conditions.

Assumption/simplification	Applicability/validity condition
Monodisperse spherical scatterers	A first-order idealization, more appropriate when scattering can be represented by a dominant effective aggregate size
$A_{ij} = 1$ normalization	Serves as an effective contrast approximation for the concrete systems considered here, rather than an exact ratio for each individual material parameter
Born approximation	Generally more reliable at lower frequencies (for example, below about 400 kHz in ordinary concrete); broader practical applicability is assessed using $k_S d_s < 10$
Exponential correlation function	Appropriate when the spatial correlation of material-property fluctuations can be reasonably represented by a monotonic decay with a single characteristic correlation length.
Diffuse-regime assumption for elastic-wave transport	Valid when multiple scattering is sufficiently strong, directional memory is largely lost, and the source-receiver spacing and analysed time windows are such that the recorded signals are dominated by diffuse coda rather than coherent or ballistic arrivals.
Rectangular cross-section approximation	Appropriate when the neglected corner voids account for only a small fraction of the total cross-sectional area

5.5. Model assumptions, validity range, and uncertainty budget

To improve the transparency of the proposed framework, Table 7 summarizes the main modelling assumptions and simplifications adopted in the present study, together with their corresponding applicability or validity conditions. This summary is intended to make explicit the conditions under which the analytical formulation is expected to provide a reasonable description of wave scattering and diffuse-wave transport in concrete.

Table 8 separates the main sources of uncertainty affecting either the predicted diffusivity or the experimentally extracted diffusivity. On the model side, material-property uncertainty is ranked as high because the sensitivity analysis presented in Fig. 3 and Table 6 shows that variations in the effective contrast parameter A_{ij} produce substantial changes in the predicted diffusivity. Aggregate-size uncertainty is ranked as uncertain because the use of a single characteristic size is likely to affect the frequency dependence of the prediction, but its quantitative contribution cannot yet be rigorously estimated within the present framework. Wave-velocity uncertainty is ranked as moderate because, although the adopted longitudinal and transverse wave velocities do affect the scattering calculation, their influence is currently less pronounced than that of the effective contrast normalization. On the experimental side, both sensor/spacing uncertainty and processing/fitting uncertainty are ranked as moderate. The former reflects the influence of source-receiver spacing, sensor coupling, and specimen-to-specimen variability on the measured coda energy and fitted diffusivity, whereas the latter reflects the influence of frequency-band selection, time-window definition, and fitting choices, particularly at high frequencies where the applicability of the Born approximation should also be checked.

6. Conclusion

In this work, a concrete-specific analytical framework for modelling body-wave scattering has been developed by explicitly tailoring multiple-scattering theory to the microstructural characteristics of concrete. Rather than treating scattering parameters as abstract statistical quantities, the framework reformulates the key inputs of scattering theory in terms of physically measurable concrete attributes within a two-phase statistical representation. This approach establishes a direct and quantitative connection between concrete microstructure, scattering cross-sections, and ultrasonic diffusivity. A key contribution of this study is the parameterization of scattering theory for concrete. In this formulation, the characteristic correlation length and material-property fluctuations are expressed in terms of geometrical and compositional descriptors, such as scatterer size, volume fraction, and matrix-scatterer property contrast. This transformation renders the total and transport scattering cross-sections practically computable for real concrete structures and converts previously abstract statistical descriptors into physically interpretable microstructural quantities. Together with the adopted normalization strategy for material-property contrasts, the framework provides a tractable and physically grounded representation of the effective scattering strength governing diffuse wave transport.

Validation across two concrete materials demonstrates the robustness and generality of the proposed framework. For geopolymer concrete, the predicted diffusivities reproduce the experimentally observed frequency dependence over the range of 50–400 kHz, indicating that coarse aggregate-dominated scattering is accurately captured. For ordinary concrete, comparison with published data confirms that the framework also describes ITZ-dominated scattering over frequencies from 100 to 900 kHz. The consistent agreement across materials and frequency ranges indicates that the dominant scattering mechanisms in concrete, whether governed by coarse aggregates or the ITZ, are captured quantitatively without relying on ad hoc fitting parameters. Overall, this work unifies concrete microstructural geometry, multiple-scattering theory, and diffuse wave transport into a single computationally accessible framework. By rendering body-wave scattering parameters directly computable from material composition, the framework provides the theoretical basis for the quantitative analysis of energy transport and equilibration in concrete. This capability is

Table 8
Uncertainty budget for the predicted and experimentally extracted diffusivity.

Uncertainty source	Representation in this study	Affected quantity	Main effect	Relative influence
Material-property uncertainty	Effective contrast represented through the $A_{ij} = 1$ normalization rather than independently measured contrasts in ρ, λ, and μ	Predicted diffusivity	Changes PSD/CPSD amplitude, scattering cross-sections, and diffusivity level	High
Wave-velocity uncertainty	Representative P-and S-wave velocities are used in the scattering and diffusion calculations	Predicted diffusivity	Affects wavenumber, dimensionless frequency, and transport cross-sections	Moderate
Aggregate-size uncertainty	Coarse aggregates represented by a single characteristic size derived from grading	Predicted diffusivity	Controls characteristic scattering scale and frequency dependence; monodisperse idealization cannot fully represent multi-scale scattering	Uncertain (potentially moderate to high)
Sensor/spacing uncertainty	Different members and sensor locations are included; spread is shown using boxplots	Extracted diffusivity	Affects measured coda energy and fitted diffusivity; overly short source-receiver spacing may prevent the signal from being fully in the diffuse regime	Moderate
Processing/fitting uncertainty	Diffusivity extracted using CWT-based decomposition, overlapping time windows, and unweighted least-squares fitting	Extracted diffusivity	Frequency-band selection, window definition, and fitting choices affect the fitted diffusivity and dissipation; at high frequencies, band selection should also be checked against the applicability of the Born approximation	Moderate

essential for advancing coda-wave-based NDT and SHM from qualitative monitoring to the quantitative interpretation of velocity changes and stress variations in concrete structures.

CRediT authorship contribution statement

Hao Cheng: Writing – original draft, Visualization, Validation, Methodology, Investigation, Formal analysis, Data curation. **Katrin Löer:** . **Max A.N. Hendriks:** Writing – review & editing, Supervision, Project administration, Funding acquisition. **Yuguang Yang:** Writing – review & editing, Supervision, Project administration, Funding acquisition, Formal analysis, Conceptualization.

Declaration of competing interest

The authors declare that they have no known competing financial interests or personal relationships that could have appeared to influence the work reported in this paper.

Appendix A. Correlation function of material-property fluctuations in two-phase material

For a two-phase material, the entirely three-dimensional space can be divided into two nonintersecting phases: Phase 1, K_1, and Phase 2, K_2. The random field of Phase 1 is:

$$I_1(\boldsymbol{x}) = \begin{cases} 1, & \text{if } \boldsymbol{x} \in K_1 \\ 0, & \text{otherwise} \end{cases} . \tag{A1}$$

Consequently, the random field of Phase 2 is $I_2(\mathbf{x}) = 1\text{-}I_1(\mathbf{x})$. The ensemble average of $I_1(\mathbf{x})$ and $I_2(\mathbf{x})$ are equivalent to the volume fraction of Phase 1 ϕ_1 and Phase 2 ϕ_2:

$$\langle I_1(\boldsymbol{x}) \rangle = \phi_1 \ , \tag{2a}$$

$$\langle I_2(\boldsymbol{x}) \rangle = \phi_2 = 1 - \phi_1 \ . \tag{2b}$$

The material density, ρ, and Lamé parameters, λ and μ, are assumed to vary spatially and to have the form [46]:

$$\rho(\boldsymbol{x}) = \overline{\rho}[1 + \delta\rho(\boldsymbol{x})] \ , \tag{3a}$$

$$\lambda(\boldsymbol{x}) = \overline{\lambda}[1 + \delta\lambda(\boldsymbol{x})] \ , \tag{3b}$$

$$\mu(\boldsymbol{x}) = \overline{\mu}[1 + \delta\mu(\boldsymbol{x})] \ , \tag{3c}$$

where terms with δ represent a dimensionless measure of the spatial fluctuations about the average. The over-bar terms are the average quantities. For example, the average density in the two-phase materials can be written as:

$$\begin{aligned} \overline{\rho} &= \langle I_1(\boldsymbol{x}) \rangle \rho_1 + \langle I_2(\boldsymbol{x}) \rangle \rho_2 \\ &= \phi_1 \rho_1 + \phi_2 \rho_2 \ , \end{aligned} \tag{A4}$$

where ρ_1 and ρ_2 are densities in Phase 1 and Phase 2, respectively. The average Lamé parameters are in the same form as the density shown in Equation (A4). Then, the spatial density of the two-phase material can be represented using the densities of Phase 1 and Phase 2 in the following form:

$$\rho(\boldsymbol{x}) = I_1(\boldsymbol{x})\rho_1 + I_2(\boldsymbol{x})\rho_2 \ . \tag{A5}$$

The following derivation will use the autocorrelation of density as an example, but the entire process applies equally to the autocorrelations of Lamé parameters or the cross-correlations of Lamé parameters and densities. The auto-correlation of the density is given by [46]:

$$R_{\rho\rho}(\boldsymbol{x} - \boldsymbol{y}) = \langle \delta\rho(\boldsymbol{x})\delta\rho(\boldsymbol{y}) \rangle \ . \tag{A6a}$$

The medium is assumed statistically isotropic and statistically homogeneous [46]. These assumptions imply that the correlation functions depend only on the magnitude of the difference of the two positions. Therefore, Equation (A6a) can be written as:

$$R_{\rho\rho}(\boldsymbol{x} - \boldsymbol{y}) = R_{\rho\rho}(|\boldsymbol{x} - \boldsymbol{y}|) = R_{\rho\rho}(r) \ , \tag{A6b}$$

where r represents the distance between two locations $\mathbf{x}$ and $\mathbf{y}$. The spatial fluctuations of density in Equation (A3a) can be written as:

$$\delta\rho(\boldsymbol{x}) = \frac{\rho(\boldsymbol{x}) - \overline{\rho}}{\overline{\rho}} \ . \tag{A7}$$

Substituting Equation (A7) into Equation (A6A) gives:

$$
\begin{aligned}
R_{\rho\rho}(\boldsymbol{r}) &= \langle \delta\rho(\boldsymbol{x})\delta\rho(\boldsymbol{y}) \rangle \\
&= \frac{\langle [\rho(\boldsymbol{x}) - \overline{\rho}\,][\rho(\boldsymbol{y}) - \overline{\rho}\,] \rangle}{\overline{\rho}^2} \\
&= \frac{\langle [\rho_1 I_1(\boldsymbol{x}) + \rho_2 I_2(\boldsymbol{x}) - \overline{\rho}\,][\rho_1 I_1(\boldsymbol{y}) + \rho_2 I_2(\boldsymbol{y}) - \overline{\rho}\,] \rangle}{\overline{\rho}^2} \\
&= \frac{\langle \rho_1^2 I_1(\boldsymbol{x}) I_1(\boldsymbol{y}) + \rho_2^2 I_2(\boldsymbol{x}) I_2(\boldsymbol{y}) + \rho_1\rho_2 [I_1(\boldsymbol{x}) I_2(\boldsymbol{y}) + I_1(\boldsymbol{y}) I_2(\boldsymbol{x})\,] \rangle}{\overline{\rho}^2} \\
&\quad - \frac{\overline{\rho}[\rho_1 \langle I_1(\boldsymbol{x}) \rangle + \rho_2 \langle I_2(\boldsymbol{x}) \rangle\,] + \overline{\rho}[\rho_1 \langle I_1(\boldsymbol{y}) \rangle + \rho_2 \langle I_2(\boldsymbol{y}) \rangle\,] - \overline{\rho}^2}{\overline{\rho}^2} \\
&= \frac{\langle \rho_1^2 I_1(\boldsymbol{x}) I_1(\boldsymbol{y}) + \rho_2^2 I_2(\boldsymbol{x}) I_2(\boldsymbol{y}) + \rho_1\rho_2 [I_1(\boldsymbol{x}) I_2(\boldsymbol{y}) + I_1(\boldsymbol{y}) I_2(\boldsymbol{x})\,] - \overline{\rho}^2 \rangle}{\overline{\rho}^2} \\
&= \frac{\langle \rho_1^2 I_1(\boldsymbol{x}) I_1(\boldsymbol{y}) + \rho_2^2 [1 - I_1(\boldsymbol{x})\,][1 - I_1(\boldsymbol{y})\,] \rangle}{\overline{\rho}^2} \\
&\quad + \frac{\langle \rho_1\rho_2 \{ I_1(\boldsymbol{x})[1 - I_1(\boldsymbol{y})\,] + I_1(\boldsymbol{y})[1 - I_1(\boldsymbol{x})\,] \} - \overline{\rho}^2 \rangle}{\overline{\rho}^2} \\
&= \frac{\left\langle (\rho_1 - \rho_2)^2 I_1(\boldsymbol{x}) I_1(\boldsymbol{y}) + \rho_2^2 + 2\rho_1\rho_2\phi_1 - 2\rho_2^2\phi_1 - [\phi_1\rho_1 + (1 - \phi_1)\rho_2\,]^2 \right\rangle}{\overline{\rho}^2} \\
&= \frac{(\rho_1 - \rho_2)^2}{\overline{\rho}^2} \langle I_1(\boldsymbol{x}) I_1(\boldsymbol{y}) - \phi_1^2 \rangle \ .
\end{aligned}
\tag{A8}
$$

Equation (A8) can be found at Eq. (8) in the article by Liu and Turner [65]. The general form of Equation (A8) refers to Equation (7) in Section 3.1. The contrast of the density for Phase 1 and Phase 2, $A_{\rho\rho}$, is defined as:

$$
A_{\rho\rho} := \frac{(\rho_1 - \rho_2)^2}{\overline{\rho}^2} \ . \tag{A9}
$$

Appendix B. Spatial Fourier transform of normalized correlation function

The spatial Fourier transform of the normalized correlation function $R(r) = \mathrm{e}^{-r/H}$ $(H > 0)$ is in the following form:

$$
\widetilde{R}(k) = \frac{1}{(2\pi)^3} \int_{\mathbb{R}^3} R(r) e^{-ikr} \mathrm{d}^3 r \ . \tag{B1}
$$

Equation (B1) can be expressed in the spherical coordinate system as:

$$
\widetilde{R}(k) = \frac{1}{(2\pi)^3} \int_0^{\infty} \int_0^{\pi} \int_0^{2\pi} e^{-\frac{r}{H}} e^{-ikr\cos\theta} r^2 \sin\theta \, \mathrm{d}\varphi \, \mathrm{d}\theta \, \mathrm{d}r \ , \tag{B2}
$$

where θ and φ are the polar angle and the azimuthal angle, respectively. Equation (B2) is similar in form to Eq. (14) in the article reported by Liu and Turner [65]. The following integral can be used to simplify Equation (B2):

$$
\int_0^{\pi} e^{-ikr\cos\theta} \sin\theta \, \mathrm{d}\theta = \frac{2\sin(kr)}{kr} \ . \tag{B3}
$$

Therefore, the analytical result of Equation (B2) is:

$$
\begin{aligned}
\widetilde{R}(k) &= \frac{1}{2k\pi^2} \int_0^{\infty} \sin(kr) r e^{-\frac{r}{H}} \mathrm{d}r \\
&= \frac{H^3}{\pi^2 \left(1 + H^2 k^2\right)^2} \ .
\end{aligned}
\tag{B4}
$$

Equation (B4) is similar in form to Eq. (17) in the article reported by Calvet and Margerin [57] and Eq. (72) in the article reported by Turner and Anugonda [46].

Appendix C. Expressions for total and transport scattering cross-sections in concrete

The expressions for total scattering cross-sections used in this paper are:

$$\Sigma_{pp} = \frac{\phi_s(1-\phi_s)H^3\omega^4}{v_p^4} \times \int_{-1}^{+1} \frac{\frac{\left(v_p^2-2v_S^2\right)^2}{v_p^4} + \frac{2\left(v_p^2-2v_S^2\right)}{v_p^2}\chi + \left[\frac{4v_S^2\left(v_p^2-2v_S^2\right)}{v_p^4}+1\right]\chi^2 + \frac{4v_S^2}{v_p^2}\chi^3 + \frac{4v_S^4}{v_p^4}\chi^4}{\left(1+2x_p^2-2x_p^2\chi\right)^2}\mathrm{d}\chi \ , \tag{C1}$$

$$\Sigma_{SS} = \frac{\phi_s(1-\phi_s)H^3\omega^4}{v_S^4}\int_{-1}^{+1}\frac{1-\chi^2+2\chi^3+2\chi^4}{\left(1+2x_S^2-2x_S^2\chi\right)^2}\mathrm{d}\chi \ , \tag{C2}$$

$$\Sigma_{PS} = \frac{\phi_s(1-\phi_s)H^3\omega^4}{v_P v_S^3}\int_{-1}^{+1}\frac{(1-\chi^2)\left(1+\frac{4v_S}{v_P}\chi+\frac{4v_S^2}{v_P^2}\chi^2\right)}{\left(1+x_P^2+x_S^2-2x_Px_S\chi\right)^2}\mathrm{d}\chi \ , \tag{C3}$$

$$\Sigma_{SP} = \frac{\phi_s(1-\phi_s)H^3\omega^4}{2v_P^3 v_S}\int_{-1}^{+1}\frac{(1-\chi^2)\left(1+\frac{4v_S}{v_P}\chi+\frac{4v_S^2}{v_P^2}\chi^2\right)}{\left(1+x_P^2+x_S^2-2x_Px_S\chi\right)^2}\mathrm{d}\chi \ . \tag{C4}$$

The weighted total scattering cross-sections can be obtained by incorporating a weighting factor of the cosine of the scattering angle in the integral used to calculate total scattering cross-sections. Therefore, the expressions for weighted total scattering cross-sections are shown as follows:

$$\Sigma_{pp}^{'} = \frac{\phi_s(1-\phi_s)H^3\omega^4}{v_p^4} \times \int_{-1}^{+1} \frac{\frac{\left(v_p^2-2v_S^2\right)^2}{v_p^4} + \frac{2\left(v_p^2-2v_S^2\right)}{v_p^2}\chi + \left[\frac{4v_S^2\left(v_p^2-2v_S^2\right)}{v_p^4}+1\right]\chi^2 + \frac{4v_S^2}{v_p^2}\chi^3 + \frac{4v_S^4}{v_p^4}\chi^4}{\left(1+2x_p^2-2x_p^2\chi\right)^2}\chi\mathrm{d}\chi \ , \tag{C5}$$

$$\Sigma_{SS}^{'} = \frac{\phi_s(1-\phi_s)H^3\omega^4}{v_S^4}\int_{-1}^{+1}\frac{1-\chi^2+2\chi^3+2\chi^4}{\left(1+2x_S^2-2x_S^2\chi\right)^2}\chi\mathrm{d}\chi \ , \tag{C6}$$

$$\Sigma_{PS}^{'} = \frac{\phi_s(1-\phi_s)H^3\omega^4}{v_P v_S^3}\int_{-1}^{+1}\frac{(1-\chi^2)\left(1+\frac{4v_S}{v_P}\chi+\frac{4v_S^2}{v_P^2}\chi^2\right)}{\left(1+x_P^2+x_S^2-2x_Px_S\chi\right)^2}\chi\mathrm{d}\chi \ , \tag{C7}$$

$$\Sigma_{SP}^{'} = \frac{\phi_s(1-\phi_s)H^3\omega^4}{2v_P^3 v_S}\int_{-1}^{+1}\frac{(1-\chi^2)\left(1+\frac{4v_S}{v_P}\chi+\frac{4v_S^2}{v_P^2}\chi^2\right)}{\left(1+x_P^2+x_S^2-2x_Px_S\chi\right)^2}\chi\mathrm{d}\chi \ . \tag{C8}$$

Appendix D. . Geometry of geopolymer concrete members and sensor layouts

This appendix presents the member geometries and the layout of sensors. The study involves three members: two prefabricated beams and a solid slab comprised of three beams. The embeddable piezoelectric sensor comprises a PZT patch, a waterproof copper package, and two protective marble blocks. The incorporation of marble blocks serves the critical purpose of shielding the delicate PZT. This sensor has a cylindrical shape with a diameter of 25 mm and a height of 20 mm. The centre frequency of this sensor is approximately 80 kHz [113]. The schematic illustration and a photo of the sensor are shown in Fig. D1. In all members, the sensors are situated at a minimum distance of 77 mm from the boundaries. Given that the frequency of interest is 50 kHz and the Rayleigh wave velocity in concrete is approximately 2300 m/s [114], the maximum effective depth of penetration for Rayleigh waves is approximately 46 mm [115]. This depth is notably smaller than the 77 mm distance, indicating that the contribution of Rayleigh wave-related energy transport in our measurements can be neglected.

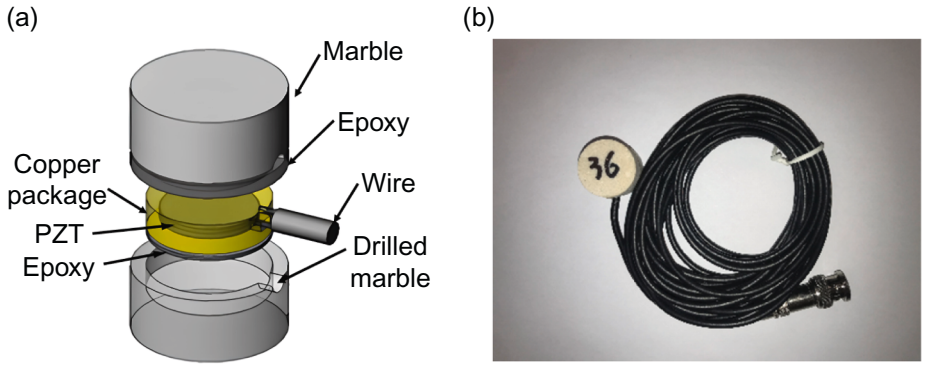

Fig. D1. Schematic and photo of an ultrasonic sensor used in this study.(a) Schematic illustration of an ultrasonic sensor [116]. (b) Photo of an ultrasonic sensor.

In the first beam, named Beam I, sensors are positioned at the mid-span. There are 12 sensors, designated from BB1 to BB12, as illustrated in Fig. D2. The specific sensor locations can be found in Table D1. Measurements are taken between adjacent sensors within each row, where the sensors in the bottom row are not in direct communication with those in the top row. There are a total of ten sensor pairs, and each sensor pair involves two measurements, swapping the roles of transmitter and receiver between the first and second measurements. Hence, a total of 20 measurements are conducted for Beam I. The input electrical signal for sensor activation is a one-cycle squared pulse with a duration of 18.5 μs and an amplitude of 200 V. The sampling rate is 3 MHz, and the maximum duration of the recorded signal is 3000 μs (9000 samples).

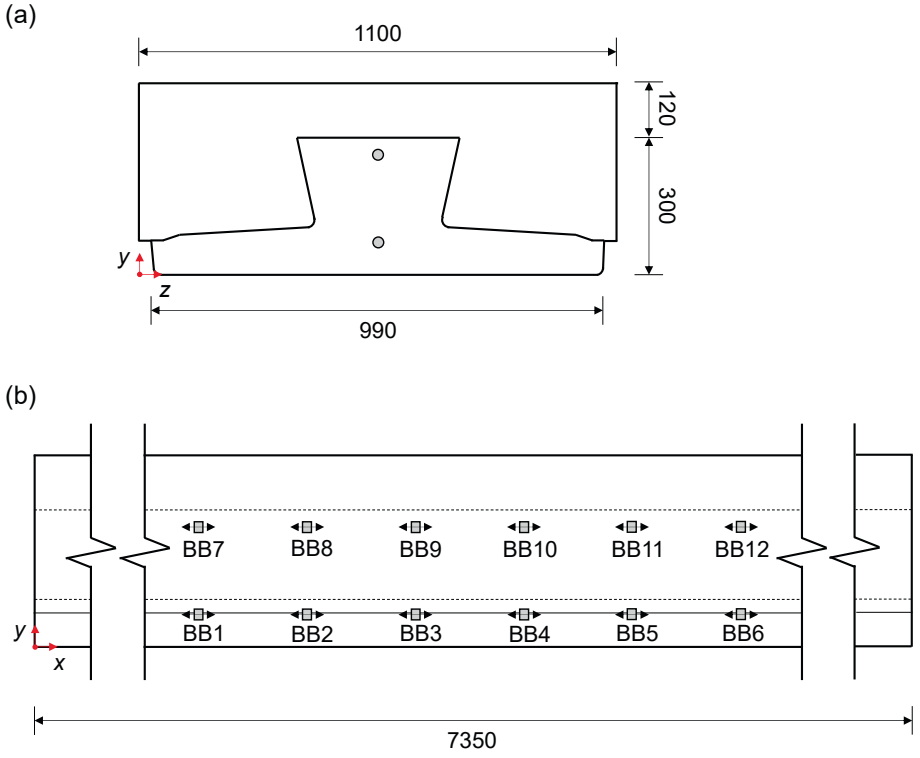

Fig. D2. Dimensions of the geopolymer concrete Beam I and the sensor layout (unit: mm; black arrow on the sensor indicates the polarization direction of the sensor). (a) Cross-sectional view. (b) Front view.

Table D1
Locations of sensors relative to the coordinates in Fig. D2.

Sensor	BB1	BB2	BB3	BB4	BB5	BB6	BB7	BB8	BB9	BB10	BB11	BB12
x [mm]	3070	3315	3560	3815	4070	4325	3070	3315	3560	3815	4070	4325
y [mm]	77	77	77	77	77	77	277	277	277	277	277	277
z [mm]	550	550	550	550	550	550	550	550	550	550	550	550

In the second beam, sensors are positioned close to the end of the beam. This specific beam, named Beam II, encompasses 12 sensors labelled from BS1 to BS12, as shown in Fig. D3. The exact sensor locations are detailed in Table D2. Similar to Beam I, measurements are performed between adjacent sensors within each row, resulting in a total of ten sensor pairs. Therefore, a total of 20 measurements are carried out for Beam II. The electrical excitation signal, sampling rate, and maximum recording duration are identical to those used in the experimental setup of Beam I.

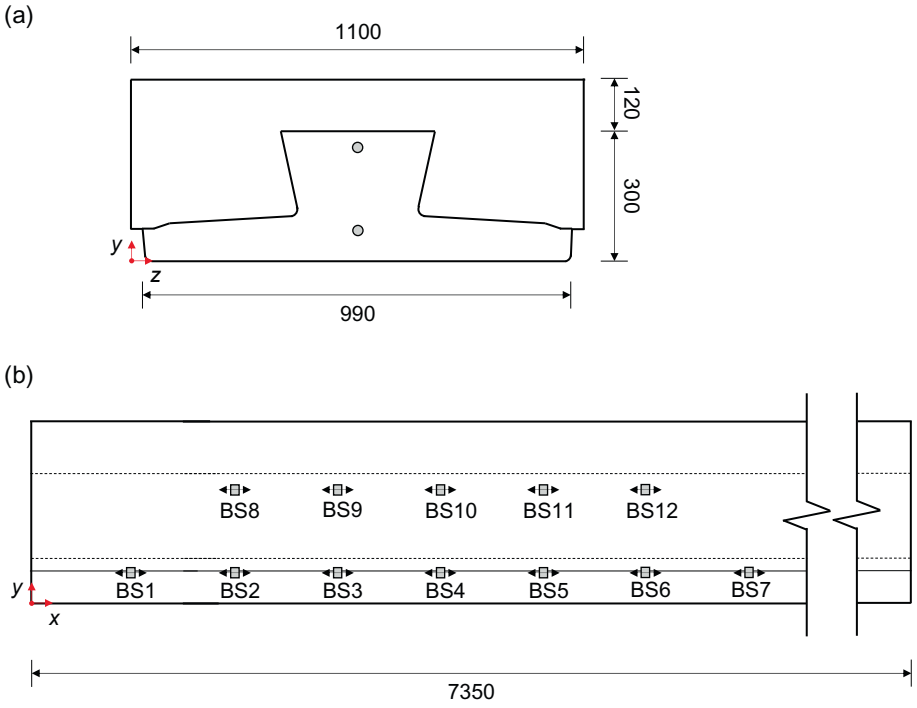

Fig. D3. Dimensions of the geopolymer concrete Beam II and the sensor layout (unit: mm; black arrow on the sensor indicates the polarization direction of the sensor). (a) Cross-sectional view. (b) Front view.

Table D2
Locations of sensors relative to the coordinates in Fig. D3.

Sensor	BS1	BS2	BS3	BS4	BS5	BS6	BS7	BS8	BS9	BS10	BS11	BS12
x [mm]	260	505	760	1015	1270	1550	1810	505	760	1015	1270	1550
y [mm]	77	77	77	77	77	77	77	277	277	277	277	277
z [mm]	550	550	550	550	550	550	550	550	550	550	550	550

The geopolymer concrete slab comprises three beams, with sensors installed in both the middle beam and one of the edge beams. In the middle beam, there are 12 sensors labelled from SB1 to SB12, illustrated in Fig. D4. The sensor locations for the middle beam can be found in Table D3. The edge beam incorporates sensors labelled from SS1 to SS10, with their respective locations detailed in Table D4. Similar to the previous beam setups, measurements are performed between adjacent sensors within each row. The electrical excitation signal, sampling rate, and maximum recording duration are identical to those used in the experimental setup of Beam I.

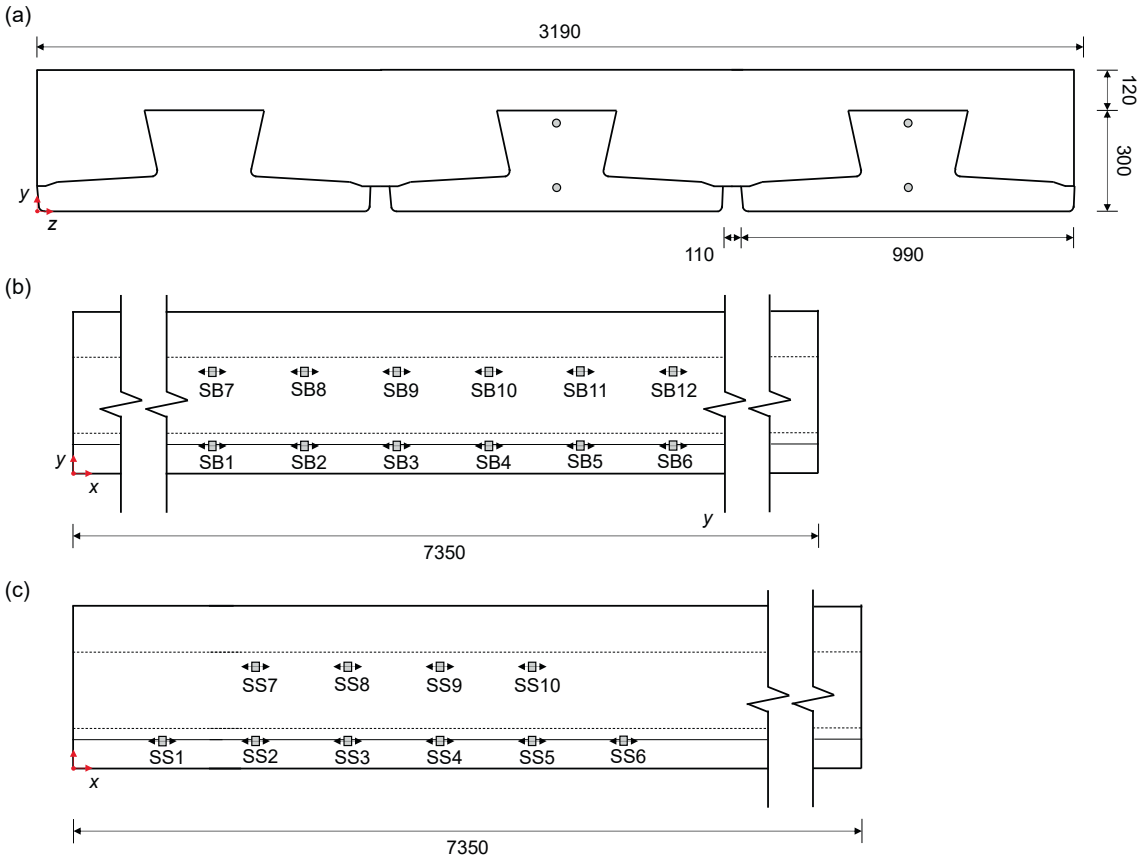

Fig. D4. Dimensions of the geopolymer concrete slab and the sensor layout (unit: mm; black arrow on the sensor indicates the polarization direction of the sensor). (a) Cross-sectional view of the slab. (b) Front view of the middle beam. (c) Front view of the edge beam.

Table D3
Locations of sensors in the middle beam relative to the coordinates in Fig. D4(a) and D4(b).

Sensor	SB1	SB2	SB3	SB4	SB5	SB6	SB7	SB8	SB9	SB10	SB11	SB12
x [mm]	3030	3290	3550	3795	4050	4300	3030	3290	3550	3795	4050	4300
y [mm]	77	77	77	77	77	77	77	277	277	277	277	277
z [mm]	1595	1595	1595	1595	1595	1595	1595	1595	1595	1595	1595	1595

Table D4
Locations of sensors in the edge beam relative to the coordinates in Fig. D4(a) and D4(c).

Sensor	SS1	SS2	SS3	SS4	SS5	SS6	SS7	SS8	SS9	SS10
x [mm]	275	535	795	1015	1265	1535	535	795	1015	1265
y [mm]	77	77	77	77	77	77	277	277	277	277
z [mm]	2695	2695	2695	2695	2695	2695	2695	2695	2695	2695

Data availability

Data will be made available on request.

References

[1] N.K. Mutlib, S. Bin Baharom, A. El-Shafie, M.Z. Nuawi, Ultrasonic health monitoring in structural engineering: buildings and bridges, Struct. Control Health Monit. 23 (3) (2016) 409–422.
[2] G. Karaiskos, A. Deraemaeker, D.G. Aggelis, D. Van Hemelrijck, Monitoring of concrete structures using the ultrasonic pulse velocity method, Smart Mater. Struct. 24 (11) (2015) 18.
[3] I.V. Tinoco, R.C.A. Pinto, Evaluation of stiffness loss of reinforced concrete beams using the diffuse ultrasound method, Ultrasonics 117 (2021) 106540.
[4] H. Hu, D. Li, L. Wang, R. Chen, X. Xu, An improved ultrasonic coda wave method for concrete behavior monitoring under various loading conditions, Ultrasonics 116 (2021) 106498.
[5] Q. Xue, E. Larose, L. Moreau, R. Thery, O. Abraham, J.M. Henault, Ultrasonic monitoring of stress and cracks of the 1/3 scale mock-up of nuclear reactor concrete containment structure, Struct. Health Monit. 21 (4) (2022) 1474–1482.
[6] B. Zhong, J. Zhu, G. Morcous, Measuring acoustoelastic coefficients for stress evaluation in concrete, Constr. Build. Mater. 309 (2021) 125127.
[7] R.L. Weaver, Diffuse elastic waves at a free surface, J. Acoust. Soc. Am. 78 (1) (1985) 131–136.
[8] Y. Lai, S.K. Cheung, Z. Zhang, Wave transport in two-dimensional random media: the ballistic to diffusive transition and the extrapolation length, Phys. Rev. E 72 (3 Pt 2) (2005) 036606.
[9] A. Derode, A. Tourin, M. Fink, Random multiple scattering of ultrasound. I. Coherent and ballistic waves, Phys. Rev. E (2001) 036605, 64(3 Pt 2.

[10] K. Aki, Analysis of the seismic coda of local earthquakes as scattered waves, J. Geophys. Res. 74 (2) (1969) 615–631.
[11] R. Snieder, A. Gret, H. Douma, J. Scales, Coda wave interferometry for estimating nonlinear behavior in seismic velocity, Science 295 (5563) (2002) 2253–2255.
[12] A. Curtis, P. Gerstoft, H. Sato, R. Snieder, K. Wapenaar, Seismic interferometry—turning noise into signal, Lead. Edge 25 (9) (2006) 1082–1092.
[13] L. Margerin, M. Campillo, B., Van Tiggelen, Monte Carlo simulation of multiple scattering of elastic waves, J. Geophys. Res.-Solid Earth 105 (B4) (2000) 7873–7892.
[14] N.P. Trégourès, B.A. van Tiggelen, Generalized diffusion equation for multiple scattered elastic waves, Waves Random Media 12 (1) (2001) 21.
[15] R. Snieder, Coda wave interferometry and the equilibration of energy in elastic media, Phys. Rev. E 66 (4 Pt 2) (2002) 046615.
[16] A. Paul, M. Campillo, L. Margerin, E. Larose, A. Derode, Empirical synthesis of time-asymmetrical Green functions from the correlation of coda waves, J. Geophys. Res.-Solid Earth 110 (B8) (2005).
[17] G.H. Watson Jr., P.A. Fleury, S.L. McCall, Searching for photon localization in the time domain, Phys. Rev. Lett. 58 (9) (1987) 945–948.
[18] D.M. Egle, Diffuse wave fields in solid media, J. Acoust. Soc. Am. 70 (2) (1981) 476–480.
[19] R.L. Weaver, On diffuse waves in solid media, J. Acoust. Soc. Am. 71 (6) (1982) 1608–1609.
[20] J.A. Turner, Scattering and diffusion of seismic waves, Bull. Seismol. Soc. Amer. 88 (1) (1998) 276–283.
[21] T. Planès, E. Larose, A review of ultrasonic Coda Wave Interferometry in concrete, Cem. Concr. Res. 53 (2013) 248–255.
[22] F. Deroo, J.Y. Kim, J. Qu, K. Sabra, L.J. Jacobs, Detection of damage in concrete using diffuse ultrasound, J. Acoust. Soc. Am. 127 (6) (2010) 3315–3318.
[23] A. Quiviger, C. Payan, J.F. Chaix, V. Garnier, J. Salin, Effect of the presence and size of a real macro-crack on diffuse ultrasound in concrete, NDT E Int. 45 (1) (2012) 128–132.
[24] C.W. In, R.B. Holland, J.Y. Kim, K.E. Kurtis, L.F. Kahn, L.J. Jacobs, Monitoring and evaluation of self-healing in concrete using diffuse ultrasound, NDT E Int. 57 (2013) 36–44.
[25] A. Quiviger, A. Girard, C. Payan, J.F. Chaix, V. Garnier, J. Salin, Influence of the depth and morphology of real cracks on diffuse ultrasound in concrete: a simulation study, NDT E Int. 60 (2013) 11–16.
[26] B. Hilloulin, J.B. Legland, E. Lys, O. Abraham, A. Loukili, F. Grondin, O. Durand, V. Tournat, Monitoring of autogenous crack healing in cementitious materials by the nonlinear modulation of ultrasonic coda waves, 3D microscopy and X-ray microtomography, Constr. Build. Mater. 123 (2016) 143–152.
[27] C.W. In, K. Arne, J.Y. Kim, K.E. Kurtis, L.J. Jacobs, Estimation of crack depth in concrete using diffuse ultrasound: validation in cracked concrete beams, J. Nondestruct. Eval. 36 (1) (2017) 1–9.
[28] C. Payan, V. Garnier, J. Moysan, P.A. Johnson, Determination of third order elastic constants in a complex solid applying coda wave interferometry, Appl. Phys. Lett. 94 (1) (2009) 3.
[29] I. Lillamand, J.F. Chaix, M.A. Ploix, V. Garnier, Acoustoelastic effect in concrete material under uni-axial compressive loading, NDT E Int. 43 (8) (2010) 655–660.
[30] S.C. Stahler, C. Sens-Schonfelder, E. Niederleithinger, Monitoring stress changes in a concrete bridge with coda wave interferometry, J. Acoust. Soc. Am. 129 (4) (2011) 1945–1952.
[31] H. Cheng, K. Löer, M.A.N. Hendriks, Y. Yang, Determining the acoustoelastic effect of longitudinal waves propagating inclined to principal stress directions in concrete: theory and experimental validation, NDT E Int. 103519 (2025).
[32] Y. Zhang, O. Abraham, F. Grondin, A. Loukili, V. Tournat, A. Le Duff, B. Lascoup, O. Durand, Study of stress-induced velocity variation in concrete under direct tensile force and monitoring of the damage level by using thermally-compensated Coda Wave Interferometry, Ultrasonics 52 (8) (2012) 1038–1045.
[33] Y. Zhang, O. Abraham, V. Tournat, A. Le Duff, B. Lascoup, A. Loukili, F. Grondin, O. Durand, Validation of a thermal bias control technique for Coda Wave Interferometry (CWI), Ultrasonics 53 (3) (2013) 658–664.
[34] M. Ramaniraka, S. Rakotonarivo, C. Payan, V. Garnier, Effect of the interfacial transition zone on ultrasonic wave attenuation and velocity in concrete, Cem. Concr. Res. 124 (2019) 105809.
[35] M. Ramaniraka, S. Rakotonarivo, C. Payan, V. Garnier, Effect of Interfacial transition Zone on diffuse ultrasound in thermally damaged concrete, Cem. Concr. Res. 152 (2022) 106680.
[36] Y. Zhang, T. Planes, E. Larose, A. Obermann, C. Rospars, G. Moreau, Diffuse ultrasound monitoring of stress and damage development on a 15-ton concrete beam, J. Acoust. Soc. Am. 139 (4) (2016) 1691.
[37] E. Niederleithinger, X. Wang, M. Herbrand, M. Muller, Processing ultrasonic data by coda wave interferometry to monitor load tests of concrete beams, Sensors 18 (6) (2018) 13.
[38] Y. Zhang, E. Larose, L. Moreau, G. d'Ozouville, Three-dimensional in-situ imaging of cracks in concrete using diffuse ultrasound, Struct. Health Monit. 17 (2) (2018) 279–284.
[39] H. Jiang, H. Zhan, Z. Ma, R. Jiang, Comparative study of three-dimensional stress and crack imaging in concrete by application of inverse algorithms to coda wave measurements, Sensors 20 (17) (2020) 4899.
[40] H. Zhan, H. Jiang, R. Jiang, Three-dimensional images generated from diffuse ultrasound wave: detections of multiple cracks in concrete structures, Struct. Health Monit. 19 (1) (2020) 12–25.
[41] R.L. Weaver, W. Sachse, Diffusion of ultrasound in a glass bead slurry, J. Acoust. Soc. Am. 97 (4) (1995) 2094–2102.
[42] R.L. Weaver, Diffusivity of ultrasound in polycrystals, J. Mech. Phys. Solids 38 (1) (1990) 55–86.
[43] L. Margerin, B. van Tiggelen, M. Campillo, Effect of absorption on energy partition of elastic waves in the seismic coda, Bull. Seismol. Soc. Amer. 91 (3) (2001) 624–627.
[44] P. Anugonda, J.S. Wiehn, J.A. Turner, Diffusion of ultrasound in concrete, Ultrasonics 39 (6) (2001) 429–435.
[45] M. Darmon, N. Khalid, M. Ramaniraka, V. Dorval, J.-M. Henault, J.-F. Chaix, Modeling of ultrasonic velocity and attenuation for concrete inspection: a review, Ultrasonics 107690 (2025).
[46] J.A. Turner, P. Anugonda, Scattering of elastic waves in heterogeneous media with local isotropy, J. Acoust. Soc. Am. 109 (5 Pt 1) (2001) 1787–1795.
[47] L. Ryzhik, G. Papanicolaou, J.B. Keller, Transport equations for elastic and other waves in random media, Wave Motion 24 (4) (1996) 327–370.
[48] P. Sheng, Introduction to wave scattering, localization and mesoscopic phenomena, Springer Science & Business Media, 2006.
[49] R.G. Newton, Scattering theory of waves and particles, Springer Science & Business Media, 2013.
[50] R.W. Boyd, A.L. Gaeta, E. Giese, Nonlinear optics, Springer Handbook of Atomic, Molecular, and Optical Physics, Springer, 2008.
[51] H. Sato, T. Hayakawa, Radiative transfer theory for a random distribution of low velocity spheres as resonant isotropic scatterers, Geophys. J. Int. 199 (1) (2014) 41–59.
[52] L. Margerin, T. Planès, J. Mayor, M. Calvet, Sensitivity kernels for coda-wave interferometry and scattering tomography: theory and numerical evaluation in two-dimensional anisotropically scattering media, Geophys. J. Int. 204 (1) (2016) 650–666.
[53] H. Sato, Temporal change in scattering and attenuation associated with the earthquake occurrence—A review of recent studies on coda waves, Pure Appl. Geophys. 126 (2) (1988) 465–497.
[54] T. Saito, H. Sato, M. Fehler, M. Ohtake, Simulating the envelope of scalar waves in 2D random media having power-law spectra of velocity fluctuation, Bull. Seismol. Soc. Amer. 93 (1) (2003) 240–252.
[55] J. Lu, S. Wang, C. Dong, Y. He, G. Tang, Heterogeneity parameters inversion from the energy of seismic scattering waves: verification from physical modelling experiments, Geophys. J. Int. 243 (3) (2025) ggaf375.
[56] K. Busch, C.M. Soukoulis, E.N. Economou, Transport and scattering mean free paths of classical waves, Phys. Rev. B 50 (1) (1994) 93–98.
[57] M. Calvet, L. Margerin, Velocity and attenuation of scalar and elastic waves in random media: a spectral function approach, J. Acoust. Soc. Am. 131 (3) (2012) 1843–1862.
[58] P. Debye, A.M. Bueche, Scattering by an Inhomogeneous Solid, J. Appl. Phys. 20 (6) (1949) 518–525.
[59] H. Frisch, Statistics of random media, Trans. Soc. Rheol. 9 (1) (1965) 293–312.
[60] C. Yeong, S. Torquato, Reconstructing random media, Phys. Rev. E 57 (1) (1998) 495.
[61] M.G. Rozman, M. Utz, Efficient reconstruction of multiphase morphologies from correlation functions, Phys. Rev. E 63 (6 Pt 2) (2001) 066701.
[62] P.S. Koutsourelakis, G. Deodatis, Simulation of binary random fields with applications to two-phase random media, J. Eng. Mech. 131 (4) (2005) 397–412.
[63] K.Z. Markov, J.R. Willis, On the two-point correlation function for dispersions of nonoverlapping spheres, Math. Mod. Meth. Appl. Sci. 8 (2) (1998) 359–377.
[64] K.Z. Markov, On the correlation functions of two-phase random media and related problems, Proceedings of the Royal Society a-Mathematical Physical and Engineering Sciences 455(1983) (1999) 1049–1066.
[65] D. Liu, J.A. Turner, Influence of spatial correlation function on attenuation of ultrasonic waves in two-phase materials, J. Acoust. Soc. Am. 123 (5) (2008) 2570–2576.
[66] S. Torquato, Exact conditions on physically realizable correlation functions of random media, J. Chem. Phys. 111 (19) (1999) 8832–8837.
[67] P. Debye, H. Anderson Jr, H. Brumberger, Scattering by an inhomogeneous solid. II. The correlation function and its application, J. Appl. Phys. 28 (6) (1957) 679–683.
[68] F.E. Stanke, Spatial autocorrelation functions for calculations of effective propagation constants in polycrystalline materials, J. Acoust. Soc. Am. 80 (5) (1986) 1479–1485.
[69] J. Spetzler, C. Sivaji, O. Nishizawa, Y. Fukushima, A test of ray theory and scattering theory based on a laboratory experiment using ultrasonic waves and numerical simulation by finite-difference method, Geophys. J. Int. 148 (2) (2002) 165–178.
[70] H. Sato, M.C. Fehler, T. Maeda, Seismic wave propagation and scattering in the heterogeneous earth, Springer, 2012.
[71] Y. Kobayashi, G. Mavko, Variation in P-wave modulus with frequency and water saturation: extension of dynamic-equivalent-medium approach, Geophysics 81 (5) (2016) D479–D494.
[72] W. Punurai, J. Jarzynski, J. Qu, J.Y. Kim, L.J. Jacobs, K.E. Kurtis, Characterization of multi-scale porosity in cement paste by advanced ultrasonic techniques, Cem. Concr. Res. 37 (1) (2007) 38–46.
[73] European Committee for Standardization, Eurocode 2: Design of concrete structures, European Committee for Standardization, 2004.
[74] M. Königsberger, M. Hlobil, B. Delsaute, S. Staquet, C. Hellmich, B. Pichler, Hydrate failure in ITZ governs concrete strength: a micro-to-macro validated engineering mechanics model, Cem. Concr. Res. 103 (2018) 77–94.
[75] G. Prokopski, J. Halbiniak, Interfacial transition zone in cementitious materials, Cem. Concr. Res. 30 (4) (2000) 579–583.

[76] Q. Chen, J. Zhang, Z. Wang, T. Zhao, Z. Wang, A review of the interfacial transition zones in concrete: identification, physical characteristics, and mechanical properties, Eng. Fract. Mech. 300 (2024) 109979.
[77] H. Alanazi, Study of the interfacial transition zone characteristics of geopolymer and conventional concretes, Gels 8 (2) (2022) 105.
[78] S. Yang, X. Guan, J. Lu, H. Cui, C.S. Poon, Micromechanical and chemical characteristics of interfacial transition zone in alkali-activated slag concrete containing lightweight iron-rich aggregates, Compos. B Eng. 283 (2024) 111671.
[79] M.P. Lutz, P.J.M. Monteiro, R.W. Zimmerman, Inhomogeneous interfacial transition zone model for the bulk modulus of mortar, Cem. Concr. Res. 27 (7) (1997) 1113–1122.
[80] G. Li, Y. Zhao, S. Pang, Four-phase sphere modeling of effective bulk modulus of concrete, Cem. Concr. Res. 29 (6) (1999) 839–845.
[81] P. Mondal, S.P. Shah, L.D. Marks, Nanomechanical Properties of Interfacial Transition Zone in Concrete, Nanotechnology in Construction 3, Proceedings 3 (2009) 315-+.
[82] D. Keinde, S. Kamali-Bernard, F. Bernard, I. Cisse, Effect of the interfacial transition zone and the nature of the matrix-aggregate interface on the overall elastic and inelastic behaviour of concrete under compression: a 3D numerical study, Eur. J. Environ. Civ. Eng. 18 (10) (2014) 1167–1176.
[83] Z. Jia, Y. Han, Y. Zhang, C. Qiu, C. Hu, Z. Li, Quantitative characterization and elastic properties of interfacial transition zone around coarse aggregate in concrete, J. Wuhan Univ. Technol.-Mater. Sci. Ed. 32 (4) (2017) 838–844.
[84] Y. Li, Y. Li, R. Wang, Quantitative evaluation of elastic modulus of concrete with nanoidentation and homogenization method, Constr. Build. Mater. 212 (2019) 295–303.
[85] G. Fang, Q. Wang, M. Zhang, Micromechanical analysis of interfacial transition zone in alkali-activated fly ash-slag concrete, Cem. Concr. Compos. 119 (2021) 103990.
[86] W. Li, H. Zhao, K. Wang, Nanocharacterization of Cementitious Composites: Unveiling Properties at Multiscale, Springer Nature, 2025.
[87] Q. Krol, H. Löwe, Relating optical and microwave grain metrics of snow: the relevance of grain shape, Cryosphere 10 (6) (2016) 2847–2863.
[88] C. Mätzler, Relation between grain-size and correlation length of snow, J. Glaciol. 48 (162) (2002) 461–466.
[89] F.F. Chen, Introduction to plasma physics and controlled fusion, Springer, 1984.
[90] M. Alderliesten, Mean particle diameters. Part V: theoretical derivation of the proper type of mean particle diameter describing a product or process property, Part. Particle Syst. Charact. 22 (4) (2005) 233–245.
[91] R. Weaver, Ultrasonics in an aluminum foam, Ultrasonics 36 (1–5) (1998) 435–442.
[92] S.K. Ramamoorthy, Y. Kane, J.A. Turner, Ultrasound diffusion for crack depth determination in concrete, J. Acoust. Soc. Am. 115 (2) (2004) 523–529.
[93] C.L. Nogueira, K.L. Rens, Acoustoelastic response of concrete under uniaxial compression, ACI Mater. J. 116 (3) (2019) 21–33.
[94] E. Ahn, M. Shin, J.S. Popovics, R.L. Weaver, Effectiveness of diffuse ultrasound for evaluation of micro-cracking damage in concrete, Cem. Concr. Res. 124 (2019) 105862.
[95] E. Ahn, M. Shin, J.S. Popovics, Air-coupled ultrasonic diffuse-wave techniques to evaluate distributed cracking damage in concrete, Ultrasonics 125 (2022) 106800.
[96] A.C.I. Committee, 225, Guide to the selection and use of hydraulic cements, Am. Concr. Instit. (2016).
[97] A.B. Malkawi, Effect of aggregate on the performance of fly-ash-based geopolymer concrete, Buildings 13 (3) (2023) 769.
[98] G. Fang, M. Zhang, The evolution of interfacial transition zone in alkali-activated fly ash-slag concrete, Cem. Concr. Res. 129 (2020) 105963.
[99] C. Hu, Z. Li, A review on the mechanical properties of cement-based materials measured by nanoindentation, Constr. Build. Mater. 90 (2015) 80–90.
[100] F.J. Ulm, M. Vandamme, C. Bobko, J. Alberto Ortega, K. Tai, C. Ortiz, Statistical indentation techniques for hydrated nanocomposites: concrete, bone, and shale, J. Am. Ceram. Soc. 90 (9) (2007) 2677–2692.
[101] F.E. Stanke, G.S. Kino, A unified theory for elastic wave-propagation in polycrystalline materials, J. Acoust. Soc. Am. 75 (3) (1984) 665–681.
[102] J.J. Sakurai, J. Napolitano, Modern quantum mechanics, Cambridge University Press, 2020.
[103] E.P. Papadakis, Ultrasonic attenuation caused by scattering in polycrystalline metals, J. Acoust. Soc. Am. 37 (4) (1965) 711–717.
[104] M. Calvet, L. Margerin, Erratum: velocity and attenuation of scalar and elastic waves in random media: a spectral function approach, J. Acoust. Soc. Am. 143 (1) (2018) 139.
[105] P.W. Anderson, The question of classical localization a theory of white paint? Philos. Mag. B 52 (3) (1985) 505–509.
[106] R.L. Weaver, Anderson localization of ultrasound, Wave Motion 12 (2) (1990) 129–142.
[107] C. Pacheco, R. Snieder, Time-lapse travel time change of multiply scattered acoustic waves, J. Acoust. Soc. Am. 118 (3) (2005) 1300–1310.
[108] A. Obermann, T. Planès, E. Larose, C. Sens-Schönfelder, M. Campillo, Depth sensitivity of seismic coda waves to velocity perturbations in an elastic heterogeneous medium, Geophys. J. Int. 194 (1) (2013) 372–382.
[109] A. Obermann, B. Froment, M. Campillo, E. Larose, T. Planès, B. Valette, J. Chen, Q. Liu, Seismic noise correlations to image structural and mechanical changes associated with the 7.9 2008 Wenchuan earthquake, J. Geophys. Res.-Solid Earth 119 (4) (2014) 3155–3168.
[110] Q. Xue, E. Larose, L. Moreau, Locating structural changes in a multiple scattering domain with an irregular shape, J. Acoust. Soc. Am. 146 (1) (2019) 595.
[111] M. Seher, C.W. In, J.Y. Kim, K.E. Kurtis, L.J. Jacobs, Numerical and experimental study of crack depth measurement in concrete using diffuse ultrasound, J. Nondestruct. Eval. 32 (1) (2013) 81–92.
[112] T. Planes, E. Larose, V. Rossetto, L. Margerin, Imaging multiple local changes in heterogeneous media with diffuse waves, J. Acoust. Soc. Am. 137 (2) (2015) 660–667.
[113] Q. Kong, Innovation in Piezoceramic Based Structural Health Monitoring, Doctoral Dissertation, University of Houston, 2015.
[114] S.W. Shin, C.B. Yun, J.S. Popovics, J.H. Kim, Improved Rayleigh wave velocity measurement for nondestructive early-age concrete monitoring, Res. Nondestruct. Eval. 18 (1) (2007) 45–68.
[115] V. Giurgiutiu, J. Bao, W. Zhao, Active sensor wave propagation health monitoring of beam and plate structures, smart structures and materials 2001: smart structures and integrated systems, Int. Soc. Opt. Photon. 2001 (2001) 234–245.
[116] L. Huo, H. Cheng, Q. Kong, X. Chen, Bond-slip monitoring of concrete structures using smart sensors-a review, Sensors 19 (5) (2019) 1231.